JGR Solid Earth

RESEARCH ARTICLE
10.1029/2025JB033164

Topography-Incorporated Adjoint-State Surface Wave Traveltime Tomography for Azimuthally Anisotropic Media

Shijie Hao[1], Jing Chen[1], Mijian Xu[2], Dayong Yu[3], Jingyun Xie[4], and Ping Tong[1,5]

[1]Division of Mathematical Sciences, School of Physical and Mathematical Sciences, Nanyang Technological University, Singapore, Singapore, [2]Department of Physics, University of Toronto, Toronto, ON, Canada, [3]School of Earth Sciences and Engineering, Nanjing University, Nanjing, China, [4]China University of Geosciences (Wuhan), Wuhan, China, [5]Earth Observatory of Singapore, Nanyang Technological University, Singapore, Singapore

Key Points:

- An anisotropic eikonal equation is proposed to model the traveltimes of surface waves in undulated, heterogeneous, and anisotropic media
- A tomography method based on the anisotropic eikonal equation is developed to directly determine shear wave velocity and anisotropy
- Low shear wave velocity and NW-oriented fast directions point to a potential hidden fault beneath the urban area of Huidong, China

Supporting Information:

Supporting Information may be found in the online version of this article.

Correspondence to:

P. Tong,
tongping@ntu.edu.sg

Citation:

Hao, S., Chen, J., Xu, M., Yu, D., Xie, J., & Tong, P. (2026). Topography-incorporated adjoint-state surface wave traveltime tomography for azimuthally anisotropic media. *Journal of Geophysical Research: Solid Earth*, *131*, e2025JB033164. https://doi.org/10.1029/2025JB033164

Received 10 OCT 2025
Accepted 25 MAR 2026

Author Contributions:

Conceptualization: Shijie Hao, Ping Tong
Data curation: Shijie Hao, Dayong Yu
Formal analysis: Shijie Hao
Funding acquisition: Dayong Yu, Ping Tong
Investigation: Shijie Hao
Methodology: Shijie Hao, Jing Chen, Mijian Xu, Ping Tong
Project administration: Ping Tong
Software: Shijie Hao, Jing Chen, Mijian Xu, Ping Tong
Supervision: Ping Tong
Validation: Shijie Hao, Jing Chen, Jingyun Xie
Visualization: Shijie Hao
Writing – original draft: Shijie Hao
Writing – review & editing: Shijie Hao, Jing Chen, Mijian Xu, Dayong Yu, Jingyun Xie, Ping Tong

Abstract Ambient noise surface wave traveltime tomography has been increasingly used to investigate shallow crustal structures. In relatively small-scale studies, factors such as topography and the uneven distribution of ambient noise sources may have significant influence on the tomographic results. In addition, anisotropy can also affect surface wave propagation, but is usually neglected. In this study, we adopt an anisotropic eikonal equation to model Rayleigh wave phase traveltime in weak anisotropic media with topographic variation. An inversion scheme is developed to invert for both shear wave velocity (Vs) and anisotropy using adjoint-state method. This tomography method is applied in the Huidong region, located near the southwestern segment of the Lianhuashan Fault Zone, China. Rayleigh wave phase delays caused by the uneven distribution of ambient noise sources are observed. This effect is corrected through traveltime correction which is determined by inverting for the azimuthal amplitude density of ambient noise. The tomographic results reveal low-Vs anomalies and ENE-oriented fast directions that are consistent with the strike of the Danshui Fault. In addition, a hidden fault is inferred from the NW-oriented fast directions and low-Vs anomalies.

Plain Language Summary Surface wave traveltime tomography is a routine technique to investigate underground structures by inverting surface wave traveltime measurements for subsurface shear wave velocity and anisotropy. Its reliability depends on accurate calculation of surface wave traveltimes. In this study, we use an anisotropic eikonal equation, incorporating the influence of velocity heterogeneity, anisotropy, and topography, to model Rayleigh wave phase traveltimes. Furthermore, the impact of unevenly distributed ambient noise sources is addressed by inverting for the ambient noise energy distribution and correcting the phase delays. This method is applied in the Huidong region, located near the southwestern segment of the Lianhuashan Fault Zone, China. The obtained low velocity anomaly and ENE-oriented anisotropy are consistent with the Danshui Fault. We found a low velocity anomaly and NW-oriented anisotropy to the north of the Danshui Fault, which may indicate a hidden fault beneath the urban area of Huidong, China.

1. Introduction

Seismic azimuthal anisotropy describes the dependence of seismic wave speeds on the azimuth of wave propagation. It can result from both present-day and historical geological processes. In the upper crust, the primary origins of seismic anisotropy include the preferential opening of cracks caused by stress field as well as structural features such as faults (Boness & Zoback, 2006; Johnson et al., 2011). Observations of seismic anisotropy serve as a valuable tool for investigating subsurface structures and stress conditions.

Anisotropy can influence the propagation of surface waves, causing ray paths to deviate from what is calculated in isotropic media. However, this effect is usually ignored in surface wave traveltime tomography (e.g., Lin et al., 2009; C. Liu et al., 2019). Eikonal equation can be used to model azimuthal anisotropy by incorporating an anisotropic term (e.g., Tong, 2021b; J. Chen et al., 2023). The elliptically anisotropic eikonal equation has been used to model surface wave traveltime and invert for surface wave velocity map (De Ridder et al., 2015; Y. Chen et al., 2023). However, the anisotropic shear wave velocity has not been obtained in these studies, limiting the ability to resolve depth-dependent variations in anisotropy. To overcome this limitation, the relationship between elliptically anisotropic eikonal equation and azimuthally anisotropic shear wave velocity needs to be addressed. In addition to seismic azimuthal anisotropy, topographic variation can also influence the propagation of seismic waves and may contribute to the azimuthal dependence of surface wave velocities (Hao et al., 2024; Du

et al., 2024; Koulakov et al., 2016; X. Zhou et al., 2023). In this work, the influence of topography is simulated by solving eikonal equation on a curved surface, following the approach of Hao et al. (2024).

On the other hand, the retrieval of empirical Green's functions from ambient noise cross-correlations relies fundamentally on the assumption of a uniform noise source distribution (V. C. Tsai, 2009; Lobkis & Weaver, 2001). Ambient noise interferometry has been widely applied to investigate crustal and upper mantle structures (e.g., Shapiro et al., 2005; G. D. Bensen et al., 2008; Kästle et al., 2018). Nevertheless, in local-scale studies, the duration of observations is often limited, and the ambient noise field may not be sufficiently diffuse. Such non-uniform noise source distributions can introduce systematic biases in traveltime measurements, potentially leading to erroneous velocity estimations and spurious anisotropy if not properly corrected (Yao & Van Der Hilst, 2009). To address this limitation, several methods have been developed. The distribution of ambient noise sources can be inferred by modeling the noise field under a plane-wave assumption (Harmon et al., 2010; K. Wang et al., 2016), or by using wave-equation-based approaches (C. Zhou et al., 2022; Datta et al., 2023). Alternatively, it has been shown that the bias caused by noise sources can be mitigated in differential time measurements (X. Liu et al., 2023; Yan et al., 2024). The impact of non-uniform noise source distributions on the inversion of azimuthal anisotropy models remains an area requiring further investigation.

One promising application of surface wave tomography is identifying hidden faults, which is crucial for earthquake hazard assessment and urban development planning (Kramer & Stewart, 2024). Several geophysical techniques have been shown to be effective to investigate hidden faults, including seismic reflection (Ishiyama et al., 2016; Reeve et al., 2015), electrical resistivity tomography (Arjwech et al., 2024; Porras et al., 2022), magnetotellurics (García et al., 2025), and gravity surveys (Dilalos & Alexopoulos, 2020; Yanis et al., 2021). In urban environments, the usage of active seismic sources is often restricted. Ambient noise tomography offers a promising alternative for delineating hidden faults by resolving both velocity and anisotropy structures. Reliable tomography results depend on accurate forward modeling. However, the effects of anisotropy, topography, and uneven distributions of ambient noise sources are frequently overlooked in surface wave traveltime tomography.

In this study, we develop a novel approach, azimuthally anisotropic adjoint-state surface wave traveltime tomography, which enables the direct inversion of surface wave traveltimes for both shear wave velocity and azimuthal anisotropy. This method utilizes an anisotropic eikonal equation to accurately model traveltime fields of surface waves in undulated, heterogeneous, and anisotropic media. The corresponding tomographic inversion problem is solved by the adjoint-state method. To reduce biases introduced by uneven ambient-noise distribution in the extracted surface-wave traveltimes, we invert for the ambient-noise amplitude density function and incorporate corresponding phase-delay corrections.

The Lianhuashan Fault Zone, the southern segment of the Zhenghe-Dapu Fault, plays a significant role in regional seismic hazard assessment and geothermal resource exploration (Lü et al., 2021; L. Liu et al., 2024; X. Li et al., 2024). However, the subsurface structure of the Lianhuashan Fault Zone remains insufficiently constrained. To address this issue, we apply our method to a large data set acquired in Huidong, China, using a dense seismic array of up to 1,110 stations. The study area covers the southwestern segment of the Lianhuashan Fault Zone, with particular focus on the Danshui Fault, which is considered the north boundary of the Lianhuashan fault zone (Xin et al., 2023). The resulting shear wave velocity and anisotropy models are compared with known fault structures and further employed to infer potential hidden faults.

2. Methodology

The adjoint-state surface wave traveltime tomography for azimuthally anisotropic media refines the shear wave velocity and anisotropy models by minimizing the misfit between observed and simulated Rayleigh wave phase traveltimes. In this section, we will discuss the following aspects in detail: (a) Simulating the traveltimes given a specific Rayleigh wave phase velocity, anisotropy and topography configuration; (b) Deriving the Fréchet derivative of the objective function with respect to Rayleigh wave phase velocity and anisotropy; (c) Deriving the Fréchet derivative of the objective function with respect to shear wave velocity and anisotropy; (d) Parameterizing and optimizing the velocity and anisotropy model.

2.1. Rayleigh Wave Phase Traveltime in Media With Azimuthal Anisotropy and Topography

In weak anisotropic media, the phase velocity of Rayleigh waves exhibits a periodicity of 180° with respect to the azimuth, characterized by mutually perpendicular fast and slow directions (Appendix B, C; Montagner & Nataf, 1986). In this case, the traveltime field can be modeled using an elliptically anisotropic eikonal equation. We consider a seismic source located at $\boldsymbol{x}_s$. The associated traveltime field T is governed by the elliptically anisotropic eikonal equation:

$$\begin{cases} \left[\nabla T(\boldsymbol{x^0})\right]^t M(\boldsymbol{x^0}) \nabla T(\boldsymbol{x^0}) = 1, \\ T(\boldsymbol{x}_s) = 0, \end{cases} \tag{1}$$

where $\boldsymbol{x^0} = (x, y)$ is any location at the Earth's surface. The matrix $M(\boldsymbol{x^0})$ represents the Rayleigh wave phase velocity and anisotropy, which are characterized by the fast velocity $c_1(\boldsymbol{x^0})$, the slow velocity $c_2(\boldsymbol{x^0})$, and the angle of the fast velocity direction counterclockwise from east $\phi(\boldsymbol{x^0})$. The eigenvalues of M correspond to the squared phase velocities along the respective eigenvector directions. Based on the fast and slow velocities and their directions, M can be expressed as:

$$M = c_1^2 \boldsymbol{p}\boldsymbol{p}^t + c_2^2 \boldsymbol{q}\boldsymbol{q}^t, \tag{2}$$

where all variables are functions of $\boldsymbol{x^0}$. $\boldsymbol{p} = (\cos\phi, \sin\phi)^t$ is the unit vector in the direction of the fast phase velocity c_1, $\boldsymbol{q} = (-\sin\phi, \cos\phi)^t$ is the unit vector in the direction of the slow phase velocity c_2.

We further consider the propagation of surface waves along an undulating surface in three-dimensional space. The surface is defined by the equation $z = \Phi(x, y)$. Similar to the case with the isotropic eikonal equation (Hao et al., 2024), corrections related to the topography can be incorporated into the elliptically anisotropic eikonal equation by projecting the traveltime gradient vector onto the tangent plane of the surface (Y.-H. R. Tsai et al., 2003). The projection operator is:

$$O_{\parallel} = I - \frac{\boldsymbol{n}\boldsymbol{n}^t}{\|\boldsymbol{n}\|^2}, \tag{3}$$

where $\boldsymbol{n}$ is the normal vector of the topography surface, given by:

$$\boldsymbol{n} = (-\Phi_x, \ -\Phi_y, \ 1)^t. \tag{4}$$

Then we extend the 2D anisotropic matrix M into 3D case (Tong, 2021b):

$$\hat{M} = c_1^2 \hat{\boldsymbol{p}}\hat{\boldsymbol{p}}^t + c_2^2 \hat{\boldsymbol{q}}\hat{\boldsymbol{q}}^t + c_3^2 \hat{\boldsymbol{r}}\hat{\boldsymbol{r}}^t, \tag{5}$$

where the fast axis $\hat{\boldsymbol{p}}$, slow axis $\hat{\boldsymbol{q}}$ and vertical axis $\hat{\boldsymbol{r}}$ are given by:

$$\hat{\boldsymbol{p}} = (\cos\phi, \sin\phi, 0)^t, \ \hat{\boldsymbol{q}} = (-\sin\phi, \cos\phi, 0)^t, \ \hat{\boldsymbol{r}} = (0, 0, 1)^t. \tag{6}$$

We define the 3D auxiliary field $\Gamma(x, y, z)$, satisfying:

$$\Gamma(x, y, z) = T(x, y), \tag{7}$$

where $T(x, y)$ represents the traveltime at the point $(x, y, \Phi(x, y))$ on the surface. Based on the assumption that surface waves propagate along the curved surface, the projection of $\nabla\Gamma$ on the tangent plane, denoted by $O_{\parallel}\nabla\Gamma$, locally describes the traveltime gradient of the surface wave. Thus, $O_{\parallel}\nabla\Gamma$ satisfies the anisotropic eikonal equation, given by:

$$\left(O_{\parallel}\nabla\Gamma\right)^{t}\hat{M}\left(O_{\parallel}\nabla\Gamma\right)=1. \tag{8}$$

Noting that $\Gamma_x = T_x$, $\Gamma_y = T_y$, and $\Gamma_z = 0$, Equation 8 reduces to:

$$\nabla T^{t}\mathcal{M}\nabla T = s^{2}, \tag{9}$$

where s represents Rayleigh wave slowness, $\mathcal{M}$ is the second-order leading principal submatrix of $s^2 O_{\parallel}^{t}\hat{M}O_{\parallel}$. We define variables $s(\boldsymbol{x}^{\mathbf{0}})$, $\xi(\boldsymbol{x}^{\mathbf{0}})$, and $\eta(\boldsymbol{x}^{\mathbf{0}})$ to describe the Rayleigh wave slowness and anisotropy as follows:

$$s=\sqrt{\frac{2}{c_1^2+c_2^2}}, \tag{10}$$

$$\xi=\frac{1}{2}\frac{c_1^2-c_2^2}{c_1^2+c_2^2}\cos 2\,\phi, \tag{11}$$

$$\eta=\frac{1}{2}\frac{c_1^2-c_2^2}{c_1^2+c_2^2}\sin 2\,\phi, \tag{12}$$

and set the vertical velocity as horizontal average by $c_3 = 1/s$. This simplification is justified as previous studies have demonstrated that the inversion results are virtually insensitive to the choice of c_3 (Eberhart-Phillips & Mark Henderson, 2004). For brevity, we further define the topographic coefficients $a(\boldsymbol{x}^{\mathbf{0}})$, $b(\boldsymbol{x}^{\mathbf{0}})$, and $c(\boldsymbol{x}^{\mathbf{0}})$ by:

$$a=\frac{1+\Phi_y^2}{\Phi_x^2+\Phi_y^2+1},\ b=\frac{1+\Phi_x^2}{\Phi_x^2+\Phi_y^2+1},\ c=\frac{\Phi_x\Phi_y}{\Phi_x^2+\Phi_y^2+1}. \tag{13}$$

Then $\mathcal{M}$ takes the explicit form:

$$\mathcal{M}=\begin{pmatrix}a & -c\\ -c & b\end{pmatrix}\begin{pmatrix}1+2\xi & 2\eta\\ 2\eta & 1-2\xi\end{pmatrix}\begin{pmatrix}a & -c\\ -c & b\end{pmatrix}+(a+b-1)\begin{pmatrix}1-a & c\\ c & 1-b\end{pmatrix}. \tag{14}$$

Figure 1a is an illustrative example of how the inclusion of anisotropy via Equation 9 can affect the traveltime field. Furthermore, we represent topography using a gridded digital elevation model, and apply a wavelength-dependent low-pass filter prior to solving the eikonal equation (Hao et al., 2024; Köhler et al., 2012). The filter removes short-wavelength variations and yields a smoother, effectively differentiable surface at the scales relevant to the surface wave wavelength. We set the corner wavelength of the filter as $\lambda_{\text{filter}} = \kappa\,\lambda_{\text{wave}}$ with $\kappa = 2.5$.

2.2. Fréchet Derivative With Respect to Phase Velocity and Anisotropy

We consider N seismic sources located at $\boldsymbol{x}_{s,n}$ ($n = 1, 2, \ldots, N$), M receivers located at $\boldsymbol{x}_{r,m}$ ($m = 1, 2, \ldots, M$), and measure the corresponding surface wave traveltime $T^{o}_{n,f}$ at frequency f ($f \in \mathcal{F}$, with $\mathcal{F}$ being the set of measured frequencies). The objective function at frequency f is defined as:

$$\chi_f=\sum_{n=1}^{N}\sum_{m=1}^{M}\frac{\omega_{n,m,f}}{2}\left[T_{n,f}(\boldsymbol{x}_{r,m})-T^{o}_{n,f}(\boldsymbol{x}_{r,m})\right]^2, \tag{15}$$

where $\omega_{n,m,f}$ is the weighting factor for each traveltime observation, $T_{n,f}(\boldsymbol{x}_{r,m})$ is the calculated traveltime between the n-th source and the m-th receiver, and $T^{o}_{n,f}(\boldsymbol{x}_{r,m})$ is the corresponding observed traveltime. The derivatives of the objective function χ_f with respect to Rayleigh wave slowness and anisotropy $\left(s_f, \xi_f, \eta_f\right)$ can be

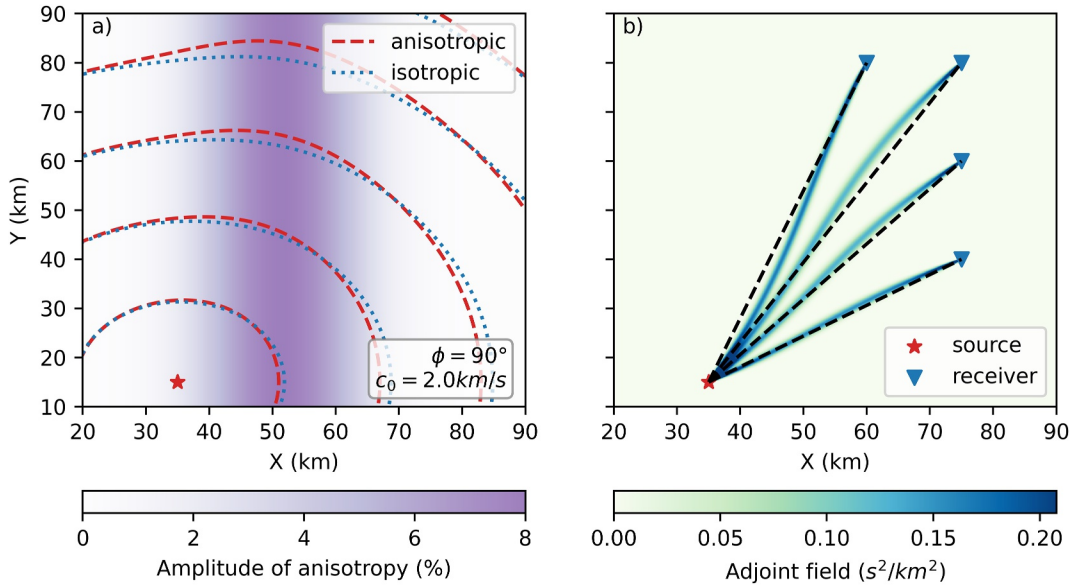

Figure 1. (a) Surface wave traveltimes in a medium with varying anisotropy and a uniform velocity. The source is denoted by the red star. The traveltime contours in the anisotropic medium are shown by the red dashed lines, while those in the corresponding isotropic medium are represented by the blue dashed lines. The amplitude of the anisotropy is depicted by the background colors. The fast velocity direction of anisotropy is 90° (along the *y*-axis). (b) The adjoint field calculated in the same anisotropic medium as in (a). The star and triangles denote the source and receivers, respectively. The black dashed lines are straight lines connecting the source and receivers, serving as a reference for how anisotropy distorts the propagation path of surface waves.

derived by the adjoint-state method (Appendix A). For brevity, the dependency of the model parameters and traveltime field on $\boldsymbol{x}^{\mathbf{0}}$ is omitted. The perturbation of the objective function can be expressed as:

$$\delta\chi_f = \int_D K_f^s \frac{\delta s_f}{s_f} d\boldsymbol{x}^{\mathbf{0}} + \int_D K_f^{\xi} \delta\xi_f d\boldsymbol{x}^{\mathbf{0}} + \int_D K_f^{\eta} \delta\eta_f d\boldsymbol{x}^{\mathbf{0}}, \tag{16}$$

where D is the study region on the Earth's surface, K_f^s, K_f^{ξ}, and K_f^{η} are surface wave slowness and anisotropy kernels defined as:

$$K_f^s = \sum_{n=1}^{N} P_{n,f} s_f^2, \tag{17}$$

$$K_f^{\xi} = \sum_{n=1}^{N} \nabla T_{n,f}^t \begin{pmatrix} a & -c \\ -c & b \end{pmatrix} \begin{pmatrix} -1 & 0 \\ 0 & 1 \end{pmatrix} \begin{pmatrix} a & -c \\ -c & b \end{pmatrix} \nabla T_{n,f} P_{n,f}, \tag{18}$$

$$K_f^{\eta} = \sum_{n=1}^{N} \nabla T_{n,f}^t \begin{pmatrix} a & -c \\ -c & b \end{pmatrix} \begin{pmatrix} 0 & -1 \\ -1 & 0 \end{pmatrix} \begin{pmatrix} a & -c \\ -c & b \end{pmatrix} \nabla T_{n,f} P_{n,f}. \tag{19}$$

$P_{n,f}$ is the adjoint field, with $P_{n,f} = 0$ on the boundary of study region, and satisfies:

$$\nabla \cdot \left\{ P_{n,f} [-\nabla T_{n,f}]^t \mathcal{M} \right\} = \sum_{m=1}^{M} \omega_{n,m,f} [T_{n,f} - T_{n,f}^o(\boldsymbol{x}_{r,m})] \delta(\boldsymbol{x} - \boldsymbol{x}_{r,m}). \tag{20}$$

The adjoint field $P_{n,f}$ in Equation 20 describes the backward transportation of the traveltime residuals from the receivers to the source. Figure 1b is an illustrative example of how the adjoint field is influenced by the inclusion

of anisotropy. Furthermore, an overall objective function is defined as the sum of the objective functions at all frequencies:

$$\chi = \sum_{f \in F} \chi_f. \tag{21}$$

2.3. Fréchet Derivative With Respect to Body Wave Velocity and Anisotropy

In a model with weak lateral heterogeneity, the propagation of surface waves can be modeled using a surface wave velocity map, where the velocity at each horizontal location is determined by the 1D depth profile of elastic parameters beneath that location, assuming the medium is laterally homogeneous within each local column (Woodhouse, 1974). This assumption is widely adopted in surface wave traveltime tomography (e.g., Bodin et al., 2012; Fang et al., 2015; Galetti et al., 2016), avoiding the substantial computational cost of solving 3D wave equations.

It is worth noting that Woodhouse (1974) incorporated topographic effects into dispersion calculations by treating surface relief as variations in local layer thickness. Similarly, Snieder (1986) formulated the influence of topography within a Born-approximation framework, modeling it as a boundary perturbation that effectively thickens or thins the local crustal waveguide, thereby altering phase velocities. In this study, we account for topography through its geometric influence on propagation by tracing surface wave paths on the curved surface. Because the geometric path effects and dispersion perturbations stem from different theoretical assumptions and are not currently unified within a consistent framework, we do not apply an additional topographic correction in dispersion curve calculation.

In a layered model, the perturbation of surface wave velocity can be expressed as a depth integration of the perturbations in 12 elastic parameters (Appendix B; Montagner & Nataf, 1986). In this study, we consider four elastic parameters, which are related to shear wave velocity (β), shear wave azimuthal anisotropy (g_c and g_s), and P-wave velocity (α). The remaining parameters, which have limited influence on Rayleigh wave phase traveltime, are fixed or treated as dependent variables (see Appendix B for details). The perturbation of Rayleigh wave phase slowness and anisotropy at the horizontal position (x, y) can be expressed as (Appendix C):

$$\delta s_f(x,y) = \int_0^\infty \left[\frac{\delta\alpha}{\alpha} K^{\alpha}_{s,f} + \frac{\delta\beta}{\beta} K^{\beta}_{s,f} + \delta g_s K^{g_s}_{s,f} + \delta g_c K^{g_c}_{s,f} \right] dz, \tag{22}$$

$$\delta \xi_f(x,y) = \int_0^\infty \left[\delta g_c K^{g_c}_{\xi,f} + \delta g_s K^{g_s}_{\xi,f} \right] dz, \tag{23}$$

$$\delta \eta_f(x,y) = \int_0^\infty \left[\delta g_c K^{g_c}_{\eta,f} + \delta g_s K^{g_s}_{\eta,f} \right] dz, \tag{24}$$

where the kernels are detailed in Equations C11–C18, the arguments (x, y, z) of both the model parameters and kernels are omitted. Finally, the perturbation of the overall objective function can be calculated by summing the perturbations of objective functions at each frequency. Substitute Equations 22–24 into Equation 16:

$$\delta\chi = \sum_{f \in F} \delta\chi_f = \int_\Omega \left[K^{\beta} \frac{\delta\beta}{\beta} + K^{\alpha} \frac{\delta\alpha}{\alpha} + K^{g_c} \delta g_c + K^{g_s} \delta g_s \right] d\boldsymbol{x}, \tag{25}$$

where the integration domain Ω denotes 3D subsurface space. Both the model parameters and their kernels are functions of location (x, y, z), which are omitted. $K^{\beta}, K^{\alpha}, K^{g_c}$, and K^{g_s} are the kernels of relative shear wave velocity, relative P-wave velocity, g_c, and g_s, respectively:

$$K^{\beta}(\boldsymbol{x}) = \sum_{f \in F} \left[\frac{1}{s_f(\boldsymbol{x^0})} K^{s}_{f}(\boldsymbol{x^0}) K^{\beta}_{s,f}(\boldsymbol{x}) \right], \tag{26}$$

$$K^{\alpha}(\boldsymbol{x}) = \sum_{f\in\mathcal{F}}\left[\frac{1}{s_f(\boldsymbol{x}^{\mathbf{0}})}K^{s}_{f}(\boldsymbol{x}^{\mathbf{0}})\,K^{\alpha}_{s,f}(\boldsymbol{x})\right], \tag{27}$$

$$K^{g}(\boldsymbol{x}) = \sum_{f\in\mathcal{F}}\left[\frac{1}{s_f(\boldsymbol{x}^{\mathbf{0}})}K^{s}_{f}(\boldsymbol{x}^{\mathbf{0}})\,K^{g}_{s,f}(\boldsymbol{x}) + K^{\xi}_{f}(\boldsymbol{x}^{\mathbf{0}})\,K^{g}_{\xi,f}(\boldsymbol{x}) + K^{\eta}_{f}(\boldsymbol{x}^{\mathbf{0}})\,K^{g}_{\eta,f}(\boldsymbol{x})\right], \tag{28}$$

$$K^{g}(\boldsymbol{x}) = \sum_{f\in\mathcal{F}}\left[\frac{1}{s_f(\boldsymbol{x}^{\mathbf{0}})}K^{s}_{f}(\boldsymbol{x}^{\mathbf{0}})\,K^{g}_{s,f}(\boldsymbol{x}) + K^{\xi}_{f}(\boldsymbol{x}^{\mathbf{0}})\,K^{g}_{\xi,f}(\boldsymbol{x}) + K^{\eta}_{f}(\boldsymbol{x}^{\mathbf{0}})\,K^{g}_{\eta,f}(\boldsymbol{x})\right]. \tag{29}$$

Note that kernels associated with body wave parameters depend on the 3D location $\boldsymbol{x} = (x, y, z)$, whereas kernels associated with surface wave parameters depend only on the horizontal location $\boldsymbol{x}^{\mathbf{0}} = (x, y)$.

The above derivation does not treat density as an independent parameter in the Fréchet derivative of the objective function Equation 25. In this study, density perturbations are assumed to scale with shear wave velocity perturbations through an empirical relationship (Montagner & Anderson, 1989; Zhu et al., 2015):

$$\frac{\delta\rho}{\rho} = 0.33\,\frac{\delta\beta}{\beta}. \tag{30}$$

2.4. Inversion Scheme

The body wave velocity and anisotropy models are discretized on a 3D regular fine grid, where the grid sizes are $\Delta x \times \Delta y \times \Delta z$. The forward modeling, which simulates Rayleigh wave phase traveltimes based on 3D body wave velocity and anisotropy models, consists of two steps. The first step is to construct anisotropic phase velocity maps at each frequency $\left(s_f(\boldsymbol{x}^{\mathbf{0}}), \xi_f(\boldsymbol{x}^{\mathbf{0}}), \eta_f(\boldsymbol{x}^{\mathbf{0}})\right)$, based on the body-wave model (Equations C5–C7). The second step is to model the traveltime field of each source by Equation 9. The anisotropic eikonal equation Equation 9 is numerically solved using the fast sweeping method (Kao et al., 2005; J. Chen et al., 2023), with the anisotropic phase slowness and traveltime field being discretized on a 2D regular fine grid, whose sizes are $\Delta x \times \Delta y$.

Based on the forward modeling described above, objective functions can be calculated. The inversion scheme minimizes the overall objective function by iteratively updating model parameters based on Equation 25. The primary target of the inversion is the anisotropic shear wave velocity, defined by the parameters β, g_c, and g_s. The P-wave velocity α can also be constrained but its kernel is generally much smaller in amplitude than that of shear wave velocity. The multiple-grid approach (Tong et al., 2019) is adopted to discretize the perturbations of anisotropic velocities $\frac{\delta\beta}{\beta}$, $\frac{\delta\alpha}{\alpha}$, δg_c, and δg_s on sparse inversion grids. The inversion grid of shear wave velocity perturbation is composed of H sets of component grids, each with $L_{h,\beta}$ grid nodes. The shear wave velocity perturbation associated with the l-th node on the h-th set of the inversion grid is denoted as $\delta C^{h}_{l,\beta}$. It is related to the continuous relative shear wave velocity perturbation $\frac{\delta\beta}{\beta}(\boldsymbol{x})$ by:

$$\frac{\delta\beta}{\beta}(\boldsymbol{x}) = \frac{1}{H}\sum_{h=1}^{H}\sum_{l=1}^{L_{h,\beta}}\delta C^{h}_{l,\beta}\,B^{h}_{l,\beta}(\boldsymbol{x}), \tag{31}$$

where $B^{h}_{l,\beta}(\boldsymbol{x})$ is a basis function associated with the l-th node on the h-th set of the inversion grid. In this study, trilinear interpolation basis functions are adopted. The inversion grid and basis function are similarly defined for parameters $\frac{\delta\alpha}{\alpha}, \delta g_c$, and δg_s:

$$\frac{\delta\alpha}{\alpha}(\boldsymbol{x}) = \frac{1}{H}\sum_{h=1}^{H}\sum_{l=1}^{L_{h,\alpha}}\delta C^{h}_{l,\alpha}\,B^{h}_{l,\alpha}(\boldsymbol{x}), \tag{32}$$

$$\delta g_c(\boldsymbol{x}) = \frac{1}{H}\sum_{h=1}^{H}\sum_{l=1}^{L_{h,g_c}}\delta C^{h}_{l,g_c}\,B^{h}_{l,g_c}(\boldsymbol{x}), \tag{33}$$

$$\delta g_s(\boldsymbol{x}) = \frac{1}{H}\sum_{h=1}^{H}\sum_{l=1}^{L_{h,g_s}} \delta C^h_{l,g_s} B^h_{l,g_s}(\boldsymbol{x}). \tag{34}$$

Substituting Equations 31–34 into Equation 25, we have:

$$\frac{\partial \chi}{\partial C^h_{l,\beta}} = \frac{1}{H}\int_\Omega K^\beta(\boldsymbol{x}) B^h_{l,\beta}(\boldsymbol{x}) d\boldsymbol{x}, \tag{35}$$

$$\frac{\partial \chi}{\partial C^h_{l,\alpha}} = \frac{1}{H}\int_\Omega K^\alpha(\boldsymbol{x}) B^h_{l,\alpha}(\boldsymbol{x}) d\boldsymbol{x}, \tag{36}$$

$$\frac{\partial \chi}{\partial C^h_{l,g_c}} = \frac{1}{H}\int_\Omega K^{g_c}(\boldsymbol{x}) B^h_{l,g_c}(\boldsymbol{x}) d\boldsymbol{x}, \tag{37}$$

$$\frac{\partial \chi}{\partial C^h_{l,g_s}} = \frac{1}{H}\int_\Omega K^{g_s}(\boldsymbol{x}) B^h_{l,g_s}(\boldsymbol{x}) d\boldsymbol{x}. \tag{38}$$

With the gradients provided in Equations 35–38, we can find an optimal vector, composed of elements $C^h_{l,\beta}$, $C^h_{l,\alpha}$, C^h_{l,g_c}, and C^h_{l,g_s}, that minimizes the objective function χ. In this study, we use the step-size-controlled gradient descent method (Tong, 2021a).

3. Application in Huidong

3.1. Data and Processing

The ambient noise data used in this study were recorded by a temporary nodal array of short period seismometers. Data acquisition was carried out in two phases: The first phase (2–16 August 2019) deployed 621 seismometers, and the second phase (20 August–5 September 2019) deployed 489 seismometers (Figure 2). The array consisted of Zland 3C and Smartsolo seismometers, both with a 5 Hz corner frequency and a sampling rate of 500 Hz.

The ambient noise processing mainly follows the procedures summarized by G. Bensen et al. (2007). Waveform data are downsampled to 50 Hz and smoothed using the moving average method in both the time and frequency domains. Cross-correlations are computed from 1-hr noise segments with a 0.5-hr overlap. To enhance signal quality, we apply the RMS-ratio selection stacking method, which has been shown to achieve an improved signal-to-noise ratio for cross-correlation functions with only tens of days of observation (Xie et al., 2020). The resulting cross-correlation functions show clear fundamental-mode Rayleigh waves in the 0.25–1 Hz band, on both the causal and non-causal parts, corresponding to stations south and north of the reference station, respectively (Figure 3). The observed asymmetry may indicate an uneven distribution of ambient noise sources (Harmon et al., 2010). We use the multiple-filter technique (Yao et al., 2006) to measure Rayleigh wave phase velocity dispersion curves on the averaged causal and acausal components, within the period range from 1.0 to 3.75 s (Figures 4a and 4b). At each frequency, we apply narrow-bandpass filtering and track waveform crests to determine Rayleigh wave phase delays. Following the far-field representation of the fundamental-mode Rayleigh wave Green's function, the phase traveltime is expressed as:

$$T^o = T^{\text{crest}} - \frac{1}{8f} + \frac{N}{f},\ N \in \mathbb{Z}, \tag{39}$$

where T^{crest} is the observed time of the waveform crest and f is the frequency. The term $-\frac{1}{8f}$ accounts for the $\frac{\pi}{4}$ phase shift in the far-field asymptotic approximation (V. C. Tsai, 2009). The integer N represents the cycle ambiguity. To prevent cycle skipping, we use a region-average dispersion curve derived from the Frequency-Bessel method as a reference (J. Wang et al., 2019). Furthermore, the inter-station distance is required to be greater than 1.5 times the surface wave wavelength at each frequency (Luo et al., 2015).

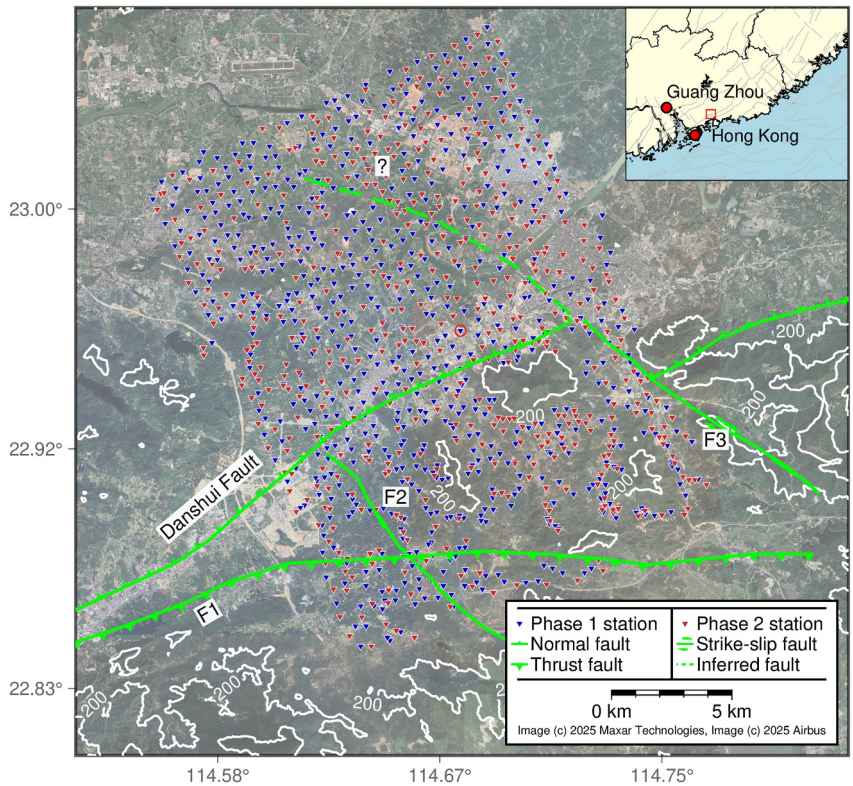

Figure 2. Satellite image with topographic contours and seismic station distribution in the Huidong region. The blue and red triangles indicate seismometers deployed in Phase 1 and Phase 2, respectively. Solid green lines represent faults identified in previous studies (J. Li et al., 2020). The dashed green line denotes a segment of a hidden fault inferred from this study. The satellite image was retrieved from Google Earth. The inset map indicates the location of the study area in southeastern China, with the red rectangle outlining the region shown in the main figure. Gray lines in the inset map represent active faults in China (Wu et al., 2024).

3.2. Noise-Source Directionality Correction

The directionality of ambient noise sources can lead to azimuthally dependent biases in phase traveltime measurements (Sadeghisorkhani et al., 2017; V. C. Tsai, 2009; Yao & Van Der Hilst, 2009), potentially resulting in

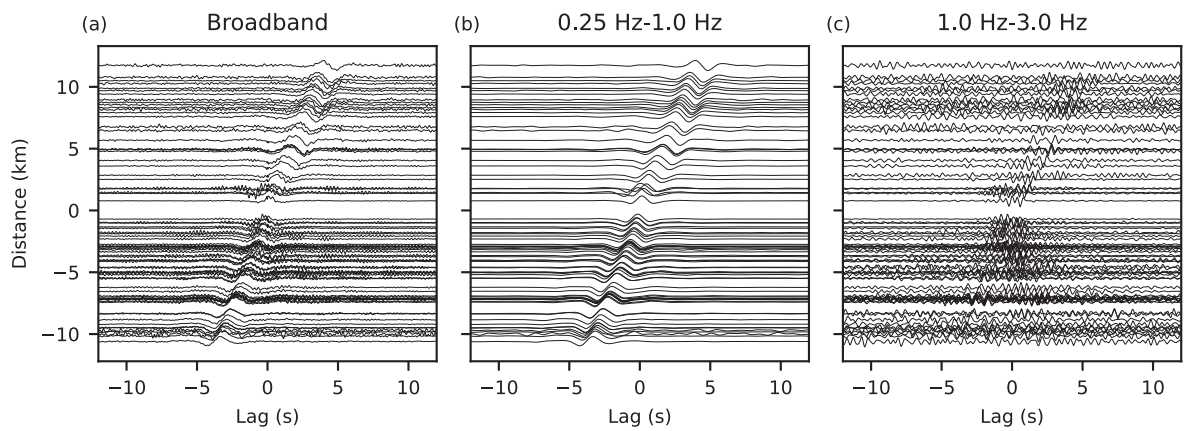

Figure 3. Cross-correlation functions calculated between the reference station (indicated by the triangle highlighted by the red circle in Figure 2) and other stations located between 114.67° and 114.69° longitude. (a)–(c) show the cross-correlation functions in (a) broadband, (b) bandpass filtered at 0.25–1 Hz, and (c) bandpass filtered at 1–3 Hz. The *y*-axis denotes the inter-station distance, with negative values indicating that the reference station is located to the north.

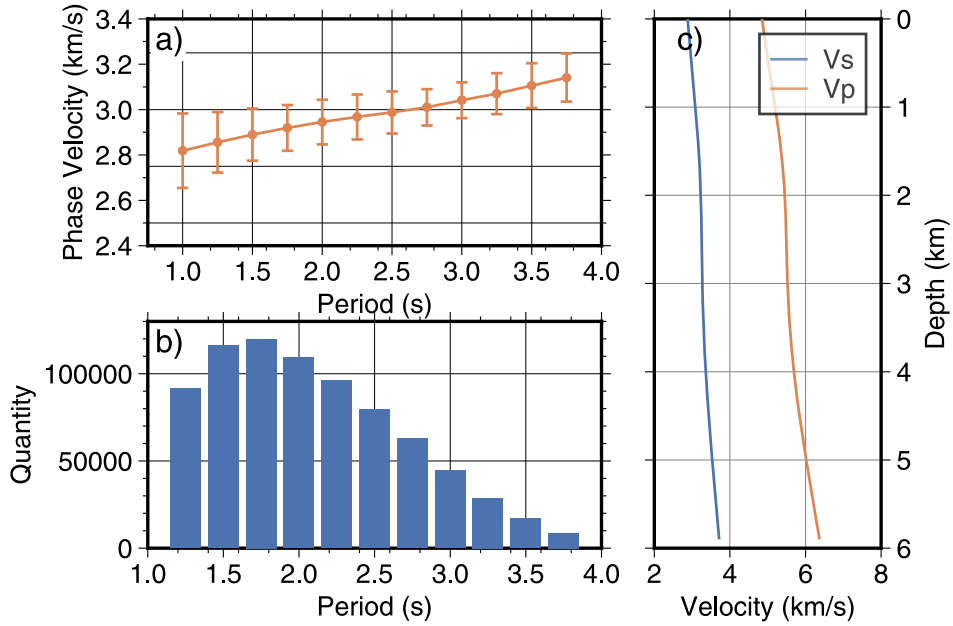

Figure 4. (a) Dispersion curves used in this study. The orange line denotes the average dispersion curve, with the corresponding standard deviations shown at each period. (b) Quantities of the dispersion curve measurements. The blue bars represent the number of dispersion curve measurements. (c) Initial velocity models.

artifacts in both velocity and azimuthal anisotropy. In this study, the observed asymmetry in the cross-correlation functions (Figure 3) suggests an uneven distribution of ambient noise sources around the study region (Harmon et al., 2010). To illustrate the systematic phase delays of surface waves at different azimuths, we invert the observed phase traveltimes for an isotropic Vs model using a procedure similar to that described in Section 3.3, and examine the residuals between isotropic-model-predicted and observed traveltimes (Figures 5b and 5c). These residuals exhibit significant azimuthal variations, which are interpreted as a consequence of the uneven

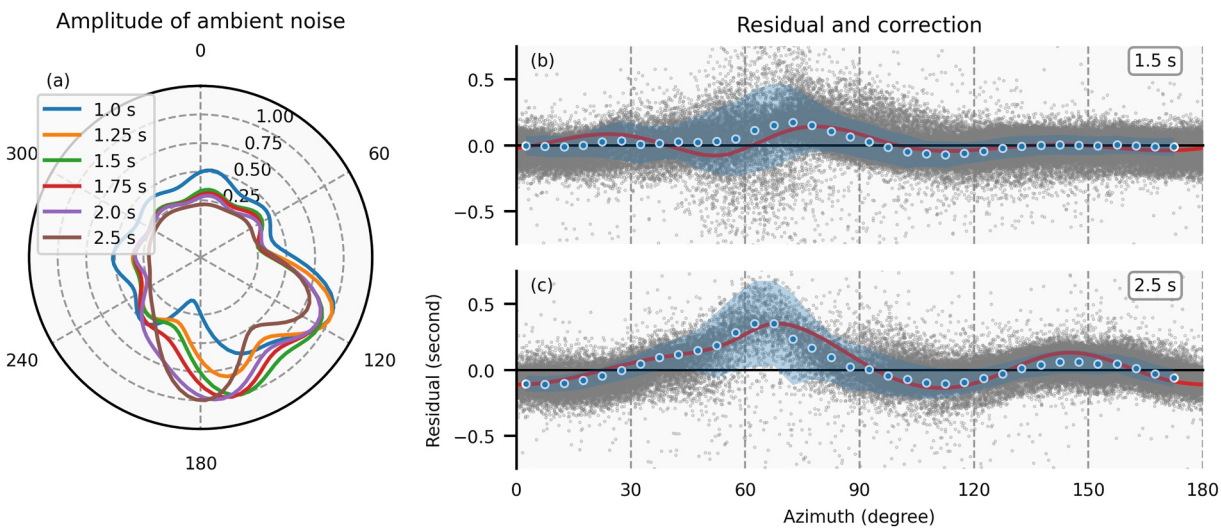

Figure 5. Inverted amplitude density of ambient noise sources and the corresponding phase delay predictions. (a) Amplitude density of ambient noise sources at periods of 1.0 s, 1.25 s, 1.5 s, 1.75 s, 2.0 s, and 2.5 s. (b) Comparison of predicted and observed traveltime deviations at 1.5 s period. The red line indicates the predicted phase delays based on the inverted amplitude density. Gray dots represent the residuals between the isotropic-model predictions and observed traveltimes. Blue dots and shaded regions represent the bin-averaged means and standard deviations, respectively, of the residuals between the final-model predictions and observations. (c) Same as (b), but for the 2.5 s period.

ambient noise source distribution. To mitigate its influence, we invert for the amplitude density of ambient noise from the frequency-domain cross-correlation functions (Appendix D; Harmon et al., 2010).

The inverted ambient noise distribution is consistent with the geographic context (Figure 5a), as the ambient noise in this period band mainly originates from oceanic waves (Nishida, 2017; Tanimoto & Anderson, 2023). Furthermore, phase delays in cross-correlation functions are predicted from the inverted ambient noise distribution (Appendix D), and can account for the observed azimuthally dependent traveltime residuals (Figures 5b and 5c). The cross-correlation functions show azimuthally dependent amplitude anomalies, which can be predicted by the inverted amplitude density function (Figures S1 and S2 in Supporting Information S1). Based on these observations, we use the inverted ambient noise distribution to correct the observed phase traveltimes before conducting anisotropic tomography. At periods longer than 2.5 s, constraining ambient noise distribution is limited by the array aperture. Therefore, the distribution estimated at 2.5 s is used for traveltime correction.

To further assess the reliability of the noise source inversion, we compared the observed traveltimes with predictions from the final heterogeneous, azimuthally anisotropic model (detailed in Section 3.3). As shown in Figures 5b and 5c, the residuals derived from this final model (blue dots) exhibit an azimuthal dependence that is consistent with those from the isotropic model (gray dots). Consequently, this validation demonstrates the robustness of our correction strategy in decoupling source-induced biases from intrinsic structural anisotropy.

3.3. Inversion and Checkerboard Resolution Test

A layered velocity model (Figure 4c) is obtained by inverting the averaged Rayleigh wave phase velocity dispersion curve (Figure 4a). This isotropic layered model serves as the initial model for the 3D tomographic inversion. The shear wave velocity and azimuthal anisotropy models are discretized on a fine grid with dimensions of $0.001^\circ \times 0.001^\circ \times 0.1$ km. P-wave velocity and density are parameterized as deterministic functions of shear wave velocity, as detailed in Hao et al. (2024). The perturbations of shear wave velocity and azimuthal anisotropy, described as a model perturbation vector $\left(\frac{\delta\beta}{\beta}, \delta g_c, \delta g_s\right)$, are interpolated on the inversion grid, which consists of 5 sets of coarse grids. The coarse grids are regular in the horizontal directions, but irregular in the vertical direction, with denser grids in the shallow depths (Figure S3 in Supporting Information S1). The irregular inversion grids in the vertical direction are designed to reflect the uneven distribution of surface wave velocity sensitivities. In addition, the inversion grid for anisotropic parameters is coarser in the horizontal directions than that for isotropic parameters (Figure S4 in Supporting Information S1), reflecting the expectation that, for a given data coverage, the resolution of anisotropic parameters is lower than that of isotropic ones.

The resulting model is obtained by iteratively updating the velocity and anisotropy models, starting from the initial layered isotropic model. Both the shear wave velocity and azimuthal anisotropy are updated simultaneously using the step-size-controlled gradient descent method (Hao et al., 2024; Tong, 2021a). At each iteration, the model perturbation vector $\left(\frac{\delta\beta}{\beta}, \delta g_c, \delta g_s\right)$ is normalized such that its maximum value equals a predefined step size. The initial step size is set to 2% and is subsequently adjusted based on the objective function. Starting from the second iteration, if the objective function increases compared to the previous iteration, indicating an overshoot due to an excessive step size, the step size is reduced to 90% of its preceding value to ensure stability. The total number of iterations is 100, where the objective function stabilizes with diminishing reductions (Figure S5 in Supporting Information S1).

Checkerboard resolution tests are conducted to evaluate the resolution of the obtained shear wave velocity and anisotropy models. Two target models are defined, featuring alternating high and low-velocity anomalies, and mutually perpendicular anisotropies (Text S1 and Figure S6 in Supporting Information S1). The inversion results for Model 1 show that the shear wave velocity anomalies and anisotropy fast directions are well recovered (Figures 6a–6c). Model 2 contains smaller velocity anomalies, and the inversion results indicate that anomalies in the southeastern corner are not well recovered, reflecting limited data coverage. The amplitudes of both the recovered velocity anomalies and azimuthal anisotropy are generally reduced compared to those in the target model. Vertical cross-sections further indicate that the depth-dependent variations of both shear wave velocity and azimuthal anisotropy are well resolved (Figure S7 in Supporting Information S1). Furthermore, we conducted a leakage test to assess potential trade-offs between isotropic velocity and azimuthal anisotropy. In this test, the target model was an isotropic model with the same shear wave velocity perturbations as that in the checkerboard

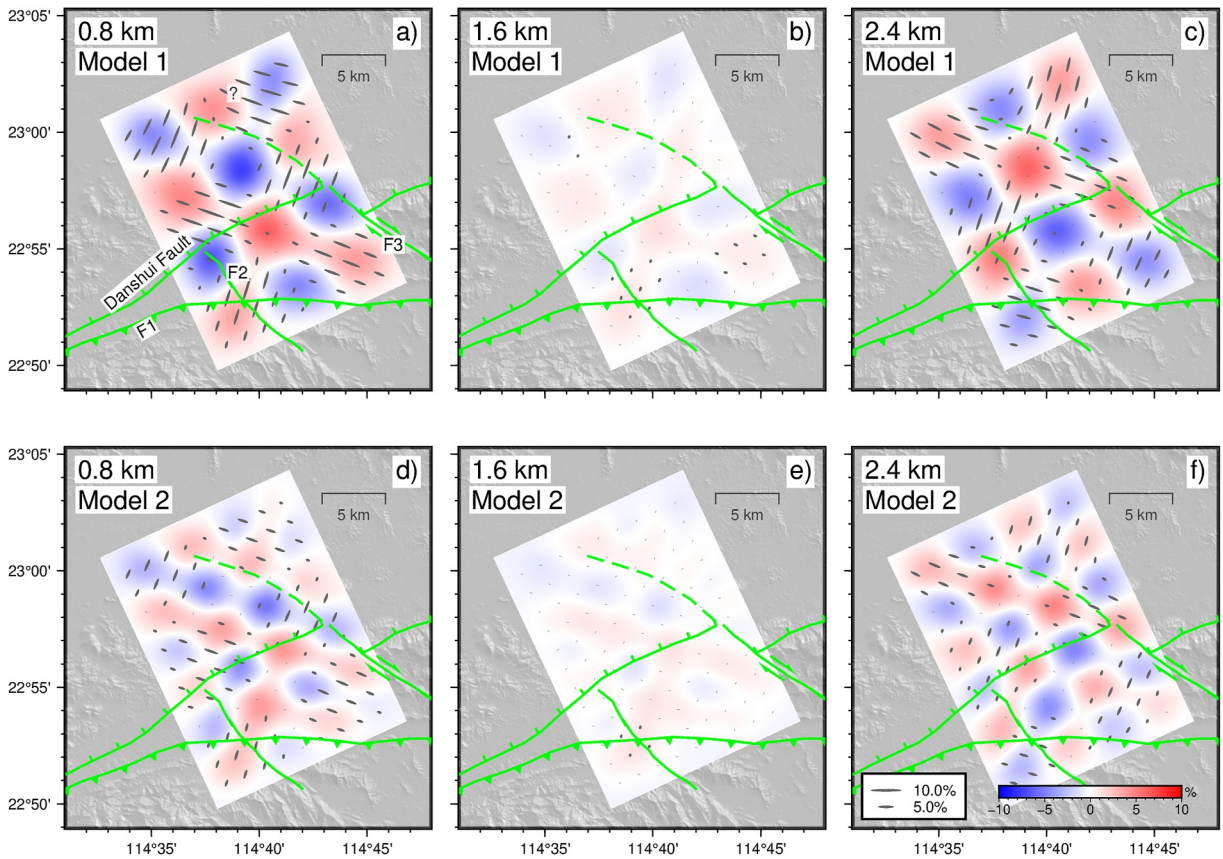

Figure 6. The recovered model of the checkerboard resolution test at depths of 0.8, 1.6 and 2.4 km. (a–c) Recovered model of target model 1. (d–f) Recovered model of target model 2. The depth is defined as the distance beneath the ground surface. The background colors denote relative shear wave velocity perturbations with respect to the average value. The directions and lengths of the gray bars indicate the fast velocity directions and amplitudes of the azimuthal anisotropy, respectively. Only anisotropies with amplitudes greater than 1% are plotted. The green lines delineate the faults as shown in Figure 2.

resolution test. Synthetic traveltimes were generated from the isotropic models and then inverted for both shear wave velocity and anisotropy using the same procedures applied to the observed data. In this test, the magnitude of the recovered anisotropy can be used to estimate the extent of leakage under the adopted parameterization and regularization. The inversion results show that the velocity perturbations are well recovered (Figure S8 in Supporting Information S1), and the amplitudes of the azimuthal anisotropies due to leakage are minor in comparison to those shown in Figure 6.

To further quantify the uncertainty and assess the statistical stability of the inversion results, we performed a random subsampling test. We generated 50 independent data realizations. Each realization was constructed by randomly retaining 80% of the unique station pairs and subsequently keeping 90% of the dispersion measurements for those selected pairs. This procedure ensures that each inversion is constrained by approximately 72% of the original data set, allowing for a simultaneous assessment of sensitivity to spatial data coverage and frequency content. These subsets were inverted using the same parameterization and regularization schemes as the final model. The evolution of the objective functions shows consistent convergence across all realizations (Figure S9 in Supporting Information S1). The resulting average model preserves the primary structural features observed in the final model (Figure S10 in Supporting Information S1). Moreover, the standard deviations for both shear wave velocity and azimuthal anisotropy are generally low in the resolved areas, confirming the robustness of the interpreted structures against variations in data coverage and measurement noise.

3.4. Tomographic Results

The resulting shear wave velocity (Vs) and azimuthal anisotropy models are shown in Figure 7, revealing complex structural features in the study region. The shallow crust is mainly composed of Jurassic to Cretaceous

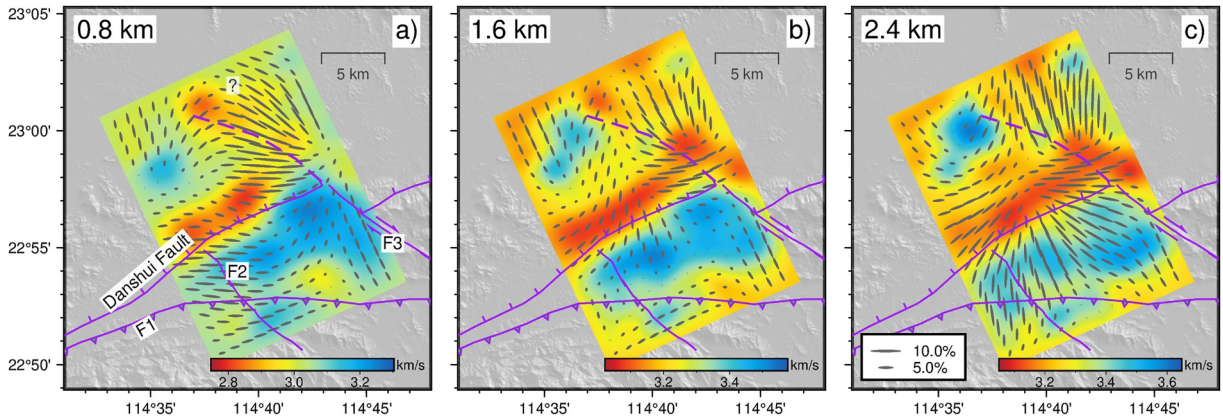

Figure 7. The resulting shear wave velocity model at depths of (a) 0.8, (b) 1.6, and (c) 2.4 km. The background colors denote the shear wave velocities, while the directions of the gray bars indicate the fast velocity directions of the shear wave azimuthal anisotropies. Only anisotropies with amplitudes greater than 1.0% are plotted. The depth is defined as the distance beneath the ground surface.

volcanic rocks (J. Li et al., 2020). Two-dimensional P-wave velocity (Vp) models derived from wide-angle seismic reflection data indicate Vp values of approximately 5.6 km/s at shallow depths (Shao-Bai et al., 2002; XiuWei et al., 2020). Our Vs model yields values of 2.8–3.3 km/s at a depth of 0.8 km (Figure 7a), consistent with the regional background. A prominent low-Vs anomaly is observed along the Danshui Fault, extending to at least 2.4 km depth (Figure 7), and is interpreted as the damage zone associated with the fault (J. Li et al., 2020). Vertical cross-sections of the final model (Figure S11 in Supporting Information S1) further reveal a NW-dipping Vs contrast across the Danshui Fault. The azimuthal anisotropy results show that at 0.8 km depth, fast directions are E in the western segment of the Danshui Fault and ENE in the eastern segment. At 1.6 km depth, the fast directions rotate to NE in the west while remaining ENE in the east. Overall, the orientation of fast directions is broadly consistent with the ENE strike of the Danshui Fault (Figures 7a and 7b).

A low-Vs anomaly is observed north of the Danshui Fault, adjacent to the segment where it is offset by the strike-slip fault F3 (Figure 7a). At the location of this low-Vs anomaly, the fast directions are oriented NW, consistent with the strike of F3. A plausible explanation for the low-Vs anomaly and NW-oriented fast directions is that the strike-slip Fault F3 extends northwestward beyond the Danshui Fault. The inferred continuation of F3 is delineated by the dashed line in Figure 7a. In the vertical cross-sections (Figure S11 in Supporting Information S1), the low-Vs anomalies and NW-oriented fast directions in the vicinity of the inferred fault can be traced to at least 2 km depth, consistent with the resolved range from the checkerboard test (Figure S7 in Supporting Information S1), but their expression weakens below this depth.

In the southernmost part of the study region, previous studies have identified two faults, F1 and F2 (J. Li et al., 2020; Xin et al., 2023). This area has experienced at least two stages of deformation, with thrust faulting followed by normal and strike-slip faulting (J. Li et al., 2020). Thrust fault F1 separates volcanic rocks to the north from sedimentary rocks to the south (Xin et al., 2023), and the juxtaposition of relatively high- and low-Vs anomalies near F1 may reflect the combined effects of earlier thrusting and subsequent strike-slip faulting.

4. Discussion

The Danshui Fault is the northern boundary of the Lianhuashan Fault Zone, with a strike of ENE (J. Li et al., 2020; Xin et al., 2023). The regional maximum horizontal compressive stress (S_{Hmax}) in the shallow crust has been determined to trend WNW based on measurements obtained using the anelastic strain recovery method (Zhang et al., 2023). In the upper crust, seismic anisotropy primarily arises from two mechanisms: stress-induced anisotropy, caused by the preferential opening or alignment of cracks under the present stress field, and structure-induced anisotropy, associated with long-lived geological features such as faults, mineral alignments, and sedimentary layering (Z. Li & Peng, 2017; Boness & Zoback, 2006). At a depth of 0.8 km, the fast directions along the Danshui Fault are E to ENE, which may reflect the influence of both fault structures and the present stress field. At depths of 1.6 and 2.4 km, the fast directions are mostly parallel to the strike of the Danshui Fault, suggesting a diminished influence of stress.

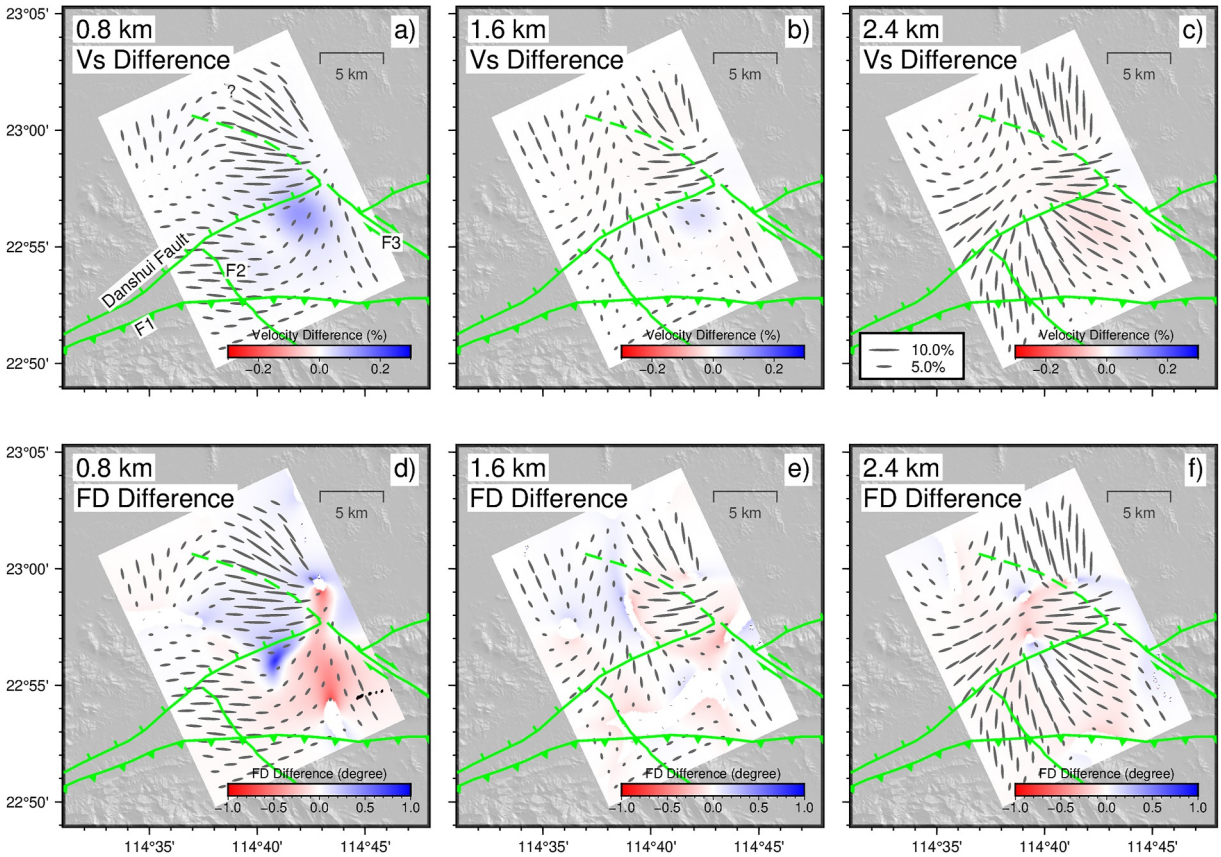

Figure 8. Estimation of shear wave velocity and anisotropy bias induced by ignoring the topographic variation. (a–c) Relative differences between Vs from tomographic inversions incorporating and ignoring topography; (d–f) Differences between fast directions from tomographic inversions incorporating and ignoring topography. The depth is defined as the distance beneath the ground surface.

Previous studies have shown that the Danshui Fault is truncated by NW-trending strike-slip faults (F3) (J. Li et al., 2020). However, to the best of our knowledge, no evidence has been reported regarding whether the strike-slip Fault F3 extends north of the Danshui Fault, where the town center of Huidong is located. In the northern part of the study region, a low Vs anomaly is observed adjacent to the position where the Danshui Fault is truncated, and extends northwestward. In addition, the fast directions are NW, consistent with the strike of F3. These observations suggest the potential existence of a NW-trending fault beneath Huidong town, which may represent a continuation of the fault F3. This inference is consistent with the regional tectonic framework. The Lianhuashan Fault Zone has undergone alternating episodes of shortening and extensional deformation (J. Li et al., 2020), and is truncated by a set of NW-trending faults (Lingyan et al., 2019). Seismicity in and around the study area is relatively low, and is primarily controlled by the NE- and NW-trending fault systems (Dai et al., 2024). Taken together, the shear-wave velocity and anisotropy patterns derived from surface wave tomography demonstrate potential for detecting and delineating hidden faults in complex tectonic settings.

One key feature of adjoint-state surface wave traveltime tomography is its capability to incorporate topographic variation. As discussed in previous research (Hao et al., 2024), ignoring the deviations in propagation paths caused by topography can lead to spurious velocity anomalies. To evaluate the influence of topography on resulting shear wave velocity and anisotropy models, we conduct a numerical test within the azimuthally anisotropic inversion by comparing tomographic results obtained with and without incorporating topography. The results show that the inclusion of topography introduces corrections to both shear wave velocity and fast direction. Specifically, overlooking topography generally leads to an underestimation of shear wave velocity, particularly beneath the major mountainous areas (Figure 8; see vertical sections in Figures S12 and S13 in Supporting Information S1). On the other hand, the impact on anisotropy is more complex, while the differences are mostly less than 1°. Overall, the numerical test suggests that the topography has limited influence in the current study area.

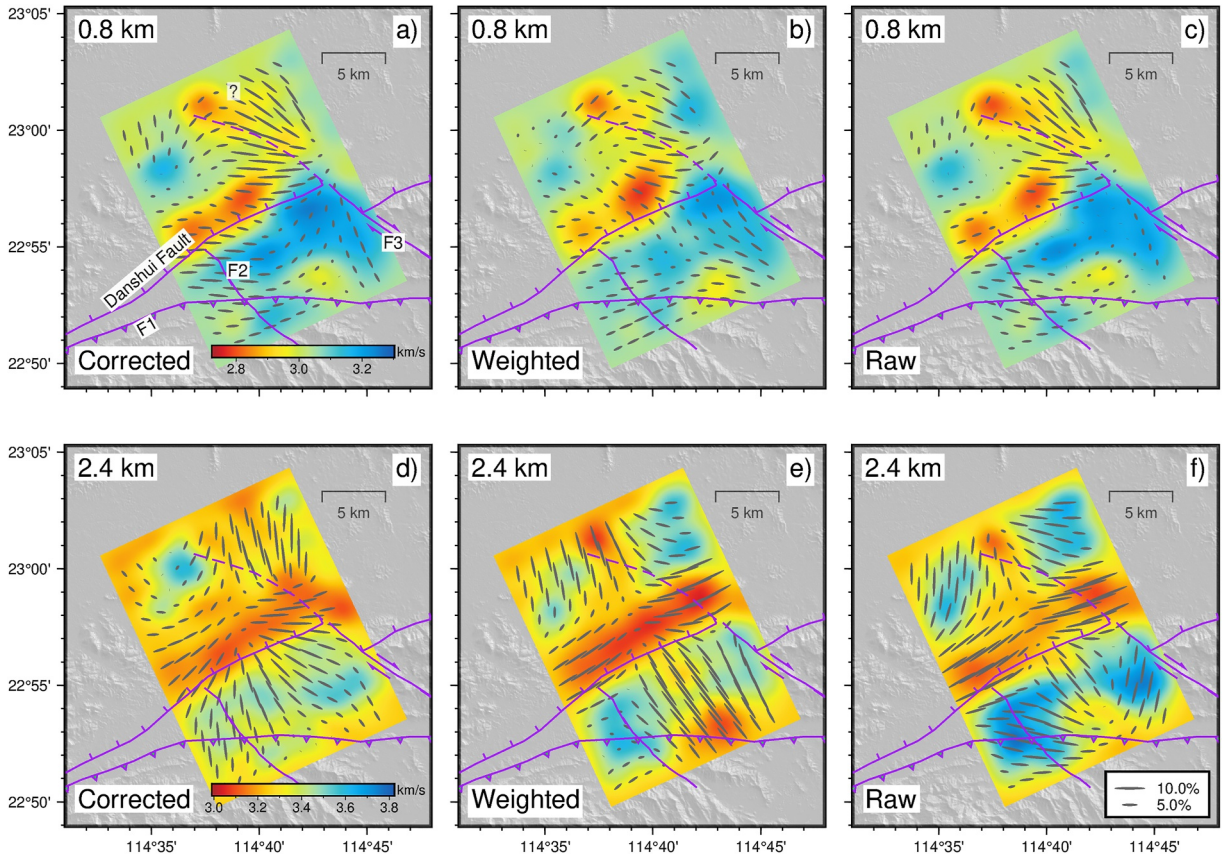

Figure 9. Comparison of resulting models using different methods for correcting phase delays caused by the uneven distribution of ambient noise sources. (a), (d) Correction using the inverted ambient noise amplitude density function; (b), (e) Azimuthally dependent weighting; (c), (f) No correction. The depth is defined as the distance beneath the ground surface.

For completeness, we provide a systematic comparison involving isotropic tomography in the Supporting Information (Figures S14–S16 in Supporting Information S1). These additional tests confirm that the misfit reduction is primarily driven by the inclusion of azimuthal anisotropy rather than topographic corrections (Figure S15 in Supporting Information S1). Furthermore, while the dominant structural patterns remain consistent, allowing for azimuthal anisotropy modifies the recovered shear wave velocity amplitudes by up to 6% compared to the isotropic inversion (Figure S16 in Supporting Information S1).

As discussed in the previous section, a challenge of using ambient noise data in this region is the uneven distribution of ambient noise sources. The modeled phase delays can reach 0.35 s at a period of 2.5 s (Figure 5), which may significantly affect the tomography results given the scale of the study area. To evaluate the impact of the ambient noise source directionality, we compare the resulting models derived from phase traveltime data with and without phase correction (Figures 9a, 9c, 9d, and 9f). As a reference, we also invert for a model using azimuthally weighted traveltime data (Figures 9b and 9e). We observed that the Rayleigh wave phase traveltime is significantly biased in certain azimuth ranges (Figures 5b and 5c). Based on these predicted phase delays, the weights are empirically selected to discard traveltime data in azimuths with significant phase bias (Table S2 in Supporting Information S1). Tomography results show that correcting for phase delays caused by unevenly distributed ambient noise sources can lead to notable differences in the anisotropy pattern, especially in greater depths (Figures 9d–9f). Furthermore, while the azimuthal weighting method yields a generally similar velocity structure to the phase correction method, notable discrepancies exist in the resolved azimuthal anisotropy. Specifically, differences in fast directions and amplitudes are observed in the northern corner above the hidden fault (Figures 9d and 9e). These differences are likely attributed to the reduction in data quantity and azimuthal coverage caused by the weighting process, which limits the constraints on azimuthal anisotropy compared to the phase correction method. Vertical cross-sections are shown in the Supporting Information (Figures S17 and S18

in Supporting Information S1) as a complementary visualization and are consistent with the map-view observations discussed above.

We have developed a software package (SurfATT) based on the adjoint-state surface wave traveltime tomography method (Hao et al., 2024; Xu et al., 2025). In our application in Huidong, the resulting model is obtained after 100 iterations, taking a total of about 47 min, utilizing 64 CPU cores (AMD EPYC 7713 up to 3.6 GHz).

5. Conclusion

In this study, we further develop adjoint-state surface wave traveltime tomography to invert for azimuthally anisotropic shear wave velocity models. We demonstrate that an elliptically anisotropic eikonal equation can be used to model Rayleigh wave phase traveltimes in weak anisotropic media. In addition, the influence of topographic variations is simulated by incorporating a topography term into the eikonal equation. An inversion scheme is then constructed by deriving the sensitivity of the objective function with respect to both shear wave velocity and anisotropy parameters using the adjoint-state method.

This method is applied in the Huidong region to invert Rayleigh wave phase traveltimes for near surface shear wave velocity and azimuthal anisotropy. Phase distortions caused by the uneven distribution of ambient noise sources are addressed by inverting for the ambient noise amplitude density function and correcting the predicted phase delays. The shear wave velocity and anisotropy patterns are consistent with local faults, particularly the Danshui Fault. In addition, a hidden fault is inferred from a low-Vs anomaly and NW-oriented fast directions.

Appendix A: Sensitivity Kernels of the Objective Function

In this section, we derive the Fréchet derivative of the objective function at a given frequency. The definitions of all variables follow those given in Section 2.2. We assume infinitesimal perturbations in the phase slowness and anisotropy parameters, denoted by $\delta s_f(\boldsymbol{x^0})$, $\delta \eta_f(\boldsymbol{x^0})$, and $\delta \xi_f(\boldsymbol{x^0})$. The resulting traveltime field perturbation is denoted by $\delta T_{n,f}(\boldsymbol{x^0})$. For brevity, the explicit dependence on $\boldsymbol{x^0}$ is omitted in the following derivation. The perturbed phase slowness, anisotropy, and traveltime field satisfy the eikonal equation:

$$[\nabla(T_{n,f}+\delta T_{n,f})]^t(\mathcal{M}+\delta\mathcal{M})\,\nabla(T_{n,f}+\delta T_{n,f})=\left(s_f+\delta s_f\right)^2, \tag{A1}$$

where $\mathcal{M}$ contains the parameters of anisotropy and topography (see Equation 14), and $\delta\mathcal{M}$ denotes the perturbation associated with anisotropy parameters, given by:

$$\delta\mathcal{M}=\begin{pmatrix} a & -c \\ -c & b \end{pmatrix}\begin{pmatrix} 2\delta\xi & 2\delta\eta \\ 2\delta\eta & -2\delta\xi \end{pmatrix}\begin{pmatrix} a & -c \\ -c & b \end{pmatrix}. \tag{A2}$$

Under the first-order approximation, the perturbation of the objective function can be expressed as:

$$\begin{aligned}\delta\chi_f &= \sum_{n=1}^{N}\sum_{m=1}^{M}\omega_{n,m,f}\left[T_{n,f}(\boldsymbol{x}_{r,m})-T^o_{n,f}(\boldsymbol{x}_{r,m})\right]\delta T_{n,f}(\boldsymbol{x}_{r,m}) \\ &= \sum_{n=1}^{N}\int_D\sum_{m=1}^{M}\omega_{n,m,f}\left[T_{n,f}(\boldsymbol{x^0})-T^o_{n,f}(\boldsymbol{x}_{r,m})\right]\delta T_{n,f}(\boldsymbol{x^0})\delta(\boldsymbol{x^0}-\boldsymbol{x}_{r,m})\,d\boldsymbol{x^0},\end{aligned} \tag{A3}$$

where D is the study region on the Earth's surface, and $\delta(\boldsymbol{x^0}-\boldsymbol{x}_{r,m})$ is the Dirac delta function. Subtracting the unperturbed eikonal equation Equation 9 from the perturbed one Equation A1 and neglecting second- and third-order terms, we obtain:

$$[\nabla T_{n,f}]^t\mathcal{M}\nabla\delta T_{n,f}=-\frac{1}{2}[\nabla T_{n,f}]^t\delta\mathcal{M}\nabla T_{n,f}+s_f\delta s_f. \tag{A4}$$

We next multiply both sides of Equation A4 by an arbitrary test function $P_{n,f}(\boldsymbol{x}^{\mathbf{0}})$ and integrate over the study region D:

$$\int_D P_{n,f}[\nabla T_{n,f}]^t \mathcal{M} \nabla \delta T_{n,f} d\boldsymbol{x}^{\mathbf{0}} = -\frac{1}{2}\int_D P_{n,f}[\nabla T_{n,f}]^t \delta\mathcal{M} \nabla T_{n,f} d\boldsymbol{x}^{\mathbf{0}} + \int_D P_{n,f} s_f \delta s_f d\boldsymbol{x}^{\mathbf{0}}. \tag{A5}$$

Assuming that $P_{n,f} = 0$ on the boundary of the study region D and applying the divergence theorem, we simplify the left-hand side of Equation A5 as follows:

$$\begin{aligned} \text{LHS} &= \int_D P_{n,f}[\nabla T_{n,f}]^t \mathcal{M} \nabla \delta T_{n,f} d\boldsymbol{x}^{\mathbf{0}} \\ &= \int_D \nabla \cdot \left\{P_{n,f}[\nabla T_{n,f}]^t \mathcal{M} \delta T_{n,f}\right\} d\boldsymbol{x}^{\mathbf{0}} - \int_D \delta T_{n,f} \nabla \cdot \left\{P_{n,f}[\nabla T_{n,f}]^t \mathcal{M}\right\} d\boldsymbol{x}^{\mathbf{0}} \\ &= \int_D \delta T_{n,f} \nabla \cdot \left\{P_{n,f}[-\nabla T_{n,f}]^t \mathcal{M}\right\} d\boldsymbol{x}^{\mathbf{0}}. \end{aligned} \tag{A6}$$

$P_{n,f}$ is an arbitrary test function for which we can make the following assumption:

$$\nabla \cdot \left\{P_{n,f}[-\nabla T_{n,f}]^t \mathcal{M}\right\} = \sum_{m=1}^{M} \omega_{n,m,f}[T_{n,f} - T^o_{n,f}(\boldsymbol{x}_{r,m})]\delta(\boldsymbol{x} - \boldsymbol{x}_{r,m}). \tag{A7}$$

Substituting Equation A7 into Equation A6, and equating the result to the right-hand side of Equation A5, we obtain:

$$\begin{aligned} &\int_D \delta T_{n,f} \sum_{m=1}^{M} \omega_{n,m,f}[T_{n,f} - T^o_{n,f}(\boldsymbol{x}_{r,m})]\delta(\boldsymbol{x} - \boldsymbol{x}_{r,m})\, d\boldsymbol{x}^{\mathbf{0}} = \\ &-\frac{1}{2}\int_D P_{n,f}[\nabla T_{n,f}]^t \delta\mathcal{M} \nabla T_{n,f} d\boldsymbol{x}^{\mathbf{0}} + \int_D P_{n,f} s_f \delta s_f d\boldsymbol{x}^{\mathbf{0}}. \end{aligned} \tag{A8}$$

We can observe from Equation A8 and Equation A3 that the perturbation of the objective function $\delta\chi_f$ can be expressed as the integration over surface wave slowness and anisotropy perturbations:

$$\begin{aligned} \delta\chi_f = &\sum_{n=1}^{N} \int_D P_{n,f} s_f \delta s_f d\boldsymbol{x}^{\mathbf{0}} \\ &+ \sum_{n=1}^{N} \int_D \nabla T^t_{n,f} \begin{pmatrix} a & -c \\ -c & b \end{pmatrix} \begin{pmatrix} -1 & 0 \\ 0 & 1 \end{pmatrix} \begin{pmatrix} a & -c \\ -c & b \end{pmatrix} \nabla T_{n,f} P_{n,f} \delta\xi_f d\boldsymbol{x}^{\mathbf{0}} \\ &+ \sum_{n=1}^{N} \int_D \nabla T^t_{n,f} \begin{pmatrix} a & -c \\ -c & b \end{pmatrix} \begin{pmatrix} 0 & -1 \\ -1 & 0 \end{pmatrix} \begin{pmatrix} a & -c \\ -c & b \end{pmatrix} \nabla T_{n,f} P_{n,f} \delta\eta_f d\boldsymbol{x}^{\mathbf{0}}. \end{aligned} \tag{A9}$$

Appendix B: Sensitivity Kernels of Azimuthally Anisotropic Rayleigh Wave Phase Velocity

A detailed derivation of the azimuthally anisotropic Rayleigh wave phase velocity and its dependence on elastic coefficients is provided in this section. In weakly anisotropic media, the directional dependence of surface wave velocity can be derived by imposing anisotropy as a perturbation on a horizontally homogeneous isotropic or transversely isotropic model (Larson et al., 1998; Montagner & Nataf, 1986; Smith & Dahlen, 1973). In the

context of Rayleigh wave phase traveltime tomography, radial anisotropy is generally not resolvable. Therefore, we derive the sensitivity kernels based on an isotropic model.

Here elastic coefficients are expressed in Voigt notation C_{ij}. In an isotropic model, the stiffness matrix is:

$$C = \begin{bmatrix} \lambda+2\mu & \lambda & \lambda & 0 & 0 & 0 \\ \lambda & \lambda+2\mu & \lambda & 0 & 0 & 0 \\ \lambda & \lambda & \lambda+2\mu & 0 & 0 & 0 \\ 0 & 0 & 0 & \mu & 0 & 0 \\ 0 & 0 & 0 & 0 & \mu & 0 \\ 0 & 0 & 0 & 0 & 0 & \mu \end{bmatrix}, \tag{B1}$$

where λ and μ are Lamé parameters. In a layered model, both parameters are functions of vertical position z. Anisotropic elastic coefficients are introduced as small perturbations γ_{ij} upon the isotropic model C_{ij}. In an isotropic horizontally homogeneous medium, the displacement of a Rayleigh wave propagating at azimuth θ (anticlockwise to the x-axis) can be expressed as:

$$\boldsymbol{u}(\boldsymbol{x},t,\theta;k,\omega) = [U(z)\cos\theta, U(z)\sin\theta, iV(z)]\, e^{i[k(x\cos\theta+y\sin\theta)-\omega t]}, \tag{B2}$$

where k is the wavenumber, $\boldsymbol{x} = (x,y,z)$ is the location, and ω is the angular frequency. The functions $U(z)$ and $V(z)$ are eigenfunctions of displacement, which can be numerically solved for a given layered model (Aki & Richards, 2002). The corresponding strain components are given below:

$$\begin{aligned}
\epsilon_1 &= \epsilon_{xx} = i\cos^2\theta k U(z) e^{i[k(x\cos\theta+y\sin\theta)-\omega t]}, \\
\epsilon_2 &= \epsilon_{yy} = i\sin^2\theta k U(z) e^{i[k(x\cos\theta+y\sin\theta)-\omega t]}, \\
\epsilon_3 &= \epsilon_{zz} = iV'(z) e^{i[k(x\cos\theta+y\sin\theta)-\omega t]}, \\
\epsilon_4 &= \epsilon_{yz} = \frac{1}{2}\sin\theta(U'(z) - kV(z))\, e^{i[k(x\cos\theta+y\sin\theta)-\omega t]}, \\
\epsilon_5 &= \epsilon_{xz} = \frac{1}{2}\cos\theta(U'(z) - kV(z))\, e^{i[k(x\cos\theta+y\sin\theta)-\omega t]}, \\
\epsilon_6 &= \epsilon_{xy} = i\cos\theta\sin\theta k U(z) e^{i[k(x\cos\theta+y\sin\theta)-\omega t]}.
\end{aligned}$$

The Lagrangian density is the difference between the kinetic energy and the elastic potential energy. For the Rayleigh wave described in Equation B2, the time-averaged Lagrangian density integrated over depth can be expressed as (Aki & Richards, 2002):

$$\mathcal{L}(C_{ij},\rho) = \frac{1}{4}\omega^2 \int_0^\infty (\rho \boldsymbol{u}\cdot\boldsymbol{u}^*)\, dz - \frac{1}{4}\int_0^\infty \left(n_{ij}C_{ij}\epsilon_i\epsilon_j^*\right) dz, \tag{B3}$$

where the superscript asterisk denotes the complex conjugate, $i,j \in \{1,2,3,4,5,6\}$, and repeated indices imply summation. The constants n_{ij} are introduced when using Voigt notation, and their values are detailed in Table B1. Averaged over time and integrated over depth, the kinetic energy equals the elastic potential energy, which leads to the condition:

$$\mathcal{L}(C_{ij},\rho) = 0. \tag{B4}$$

For a given wavenumber, we introduce perturbations to the elastic coefficients, leading to corresponding perturbations of the angular frequency and eigenfunctions. The condition in Equation B4 remains valid for the perturbed model:

Table B1
Real Part of $\gamma_{ij}\epsilon_i\epsilon_j^*$ for Rayleigh Waves. S and C Denote sin θ and cos θ, Respectively

ij	n_{ij}	$\mathrm{Re}\left(\gamma_{ij}\epsilon_i\epsilon_j^*\right)$
11	1	$C^4k^2U^2\gamma_{11}$
12	2	$C^2S^2k^2U^2\gamma_{12}$
13	2	$C^2kUV'\gamma_{13}$
14	4	0
15	4	0
16	4	$C^3Sk^2U^2\gamma_{16}$
22	1	$S^4k^2U^2\gamma_{22}$
23	2	$S^2kUV'\gamma_{23}$
24	4	0
25	4	0
26	4	$CS^3k^2U^2\gamma_{26}$
33	1	$V'^2\gamma_{33}$
34	4	0
35	4	0
36	4	$CSkUV'\gamma_{36}$
44	4	$\frac{1}{4}S^2(U' - kV)^2\gamma_{44}$
45	8	$\frac{1}{4}CS(U' - kV)^2\gamma_{45}$
46	8	0
55	4	$\frac{1}{4}C^2(U' - kV)^2\gamma_{55}$
56	8	0
66	4	$C^2S^2k^2U^2\gamma_{66}$

$$\mathcal{L}\left(C_{ij} + \gamma_{ij}, \rho\right) = 0. \tag{B5}$$

According to Rayleigh's principle, the Lagrangian density $\mathcal{L}$ is stationary with respect to small perturbations in eigenfunctions δU and δV (Smith & Dahlen, 1973). Subtracting Equation B4 from Equation B5, and retaining only first-order terms:

$$\delta\left(\omega^2\right)\int_0^\infty (\rho\boldsymbol{u}\cdot\boldsymbol{u}^*)\,dz = \int_0^\infty \left(n_{ij}\gamma_{ij}\epsilon_i\epsilon_j^*\right)dz. \tag{B6}$$

Based on the relationship between phase velocity and angular frequency $c = \frac{\omega}{k}$, the perturbation of phase velocity can be expressed as:

$$\delta c = \frac{c_0}{2\omega^2}\frac{\int_0^\infty \left(n_{ij}\gamma_{ij}\epsilon_i\epsilon_j^*\right)dz}{\int_0^\infty (\rho\boldsymbol{u}\cdot\boldsymbol{u}^*)\,dz}, \tag{B7}$$

where c_0 is the Rayleigh wave phase velocity in the unperturbed isotropic velocity model. The values of $n_{ij}\gamma_{ij}\epsilon_i\epsilon_j^*$ are listed in Table B1. This expression shows that the phase velocity perturbation can be formulated as the integral of the elastic coefficient perturbations γ_{ij}. The $\sin\theta$ and $\cos\theta$ terms can be further simplified using the power reduction identities, resulting in a combination of constant, $\sin 2\theta$, $\sin 4\theta$, $\cos 2\theta$, and $\cos 4\theta$. The perturbation of phase velocity can be further expressed as:

$$\delta c(\omega,\theta) = \sum_{p\in\mathcal{P}}\int_0^\infty p(z)K_c^p(\omega,z)f^p(\theta)dz, \tag{B8}$$

where p represents linear combinations of the elastic coefficient perturbations γ_{ij}, K_c^p is the corresponding sensitivity kernel, and $f^p(\theta)$ is the azimuthal dependence term. The values of $p\in\mathcal{P}$, K_c^p, and $f^p(\theta)$ are enumerated in Table B2. For a given velocity model, the eigenfunctions $U(z)$ and $V(z)$ are determined, and the wavenumber k is dependent on the angular frequency ω. Consequently, the sensitivity kernels K_c^p depend only on ω and z.

The parameters A, C, F, L, G_c, G_s, B_c, B_s, H_c, H_s, C_c and C_s are defined following previous research (e.g., Montagner & Nataf, 1986; M. Chen & Tromp, 2007). Their relationship with body wave velocities is summarized by M. Chen and Tromp (2007). The parameters A, C and F are related to the velocities of body waves at different incidence angles and polarizations, while H_c and H_s describe the azimuthal dependence of F. In the context of Rayleigh wave phase traveltime tomography, we assume that body wave velocities are identical at different incidence angles, leading to the following relationships: $A = C, F = A - 2L$, and $H_c = H_s = 0$. The parameters B_c and B_s describe the azimuthal dependence of horizontally propagating P-wave velocities. We assume $B_c = G_c$ and $B_s = G_s$, indicating that horizontally propagating P-waves have the same fast direction as that of shear waves. This assumption is reasonable as the fast directions of both P-waves and shear waves can be governed by common structural features such as foliation (Almqvist & Mainprice, 2017). The parameters C_c and C_s represent azimuthal terms associated with $\cos 4\theta$ and $\sin 4\theta$, respectively, and are usually considered negligible (Montagner & Nataf, 1986). Based on these assumptions, the perturbation of Rayleigh wave phase velocity depends only on the perturbations of four parameters: A, L, G_c, and G_s. The parameter A is related to the velocity of horizontally propagating P-waves (denoted by α) by $A = \rho\alpha^2$, L is related to the velocity of horizontally propagating, vertically polarized shear waves (denoted by β) by $L = \rho\beta^2$. Furthermore, each elastic parameter is related to a dimensionless parameter by the following relationship:

$$\frac{\delta\alpha}{\alpha} = \frac{\delta A}{2A}, \tag{B9}$$

Table B2
Elastic Parameters, Corresponding Sensitivity Kernels, and Their Azimuthal Dependence. All Elastic Coefficients in the First Column, as Well as the Eigenfunctions U and V, are Functions of Depth

$p(z)$	$K_c^p(\omega,z)$	$f^p(\theta)$
$\delta A = \frac{3}{8}(\gamma_{11}+\gamma_{22}) + \frac{1}{4}\gamma_{12} + \frac{1}{2}\gamma_{66}$	$K_0k^2U^2$	1
$\delta C = \gamma_{33}$	$K_0V'^2$	1
$\delta F = \frac{1}{2}(\gamma_{13}+\gamma_{23})$	$2K_0kUV'$	1
$\delta L = \frac{1}{2}(\gamma_{44}+\gamma_{55})$	$K_0(U'-kV)^2$	1
$\delta G_c = \frac{1}{2}(\gamma_{55}-\gamma_{44})$	$K_0(U'-kV)^2$	$\cos 2\theta$
$\delta G_s = \gamma_{45}$	$K_0(U'-kV)^2$	$\sin 2\theta$
$\delta B_c = \frac{1}{2}(\gamma_{11}-\gamma_{22})$	$K_0k^2U^2$	$\cos 2\theta$
$\delta B_s = \gamma_{16}+\gamma_{26}$	$K_0k^2U^2$	$\sin 2\theta$
$\delta H_c = \frac{1}{2}(\gamma_{13}-\gamma_{23})$	$2K_0kUV'$	$\cos 2\theta$
$\delta H_s = \gamma_{36}$	$2K_0kUV'$	$\sin 2\theta$
$\delta C_c = \frac{1}{8}(\gamma_{11}+\gamma_{22}) - \frac{1}{4}\gamma_{12} - \frac{1}{2}\gamma_{66}$	$K_0k^2U^2$	$\cos 4\theta$
$\delta C_s = \frac{1}{2}(\gamma_{16}-\gamma_{26})$	$K_0k^2U^2$	$\sin 4\theta$

Note. $K_0 = c/\left[2\omega^2\int_0^\infty \rho(U^2+V^2)\,dz\right]$ is a constant for a given reference model.

$$\frac{\delta\beta}{\beta} = \frac{\delta L}{2L}, \tag{B10}$$

$$\delta g_c = \frac{\delta G_c}{2L}, \tag{B11}$$

$$\delta g_s = \frac{\delta G_s}{2L}. \tag{B12}$$

The direction and amplitude of the fast shear wave velocity can be calculated by $\phi_\beta = \frac{1}{2}\arctan\frac{g_s}{g_c}$ and $A_\beta = \sqrt{g_s^2+g_c^2}$, respectively. Finally, the perturbation of Rayleigh wave phase velocity can be expressed as:

$$\begin{aligned}\delta c(\omega,\theta) = \int_0^\infty \Big[&\frac{\delta\alpha}{\alpha}(z)K_c^\alpha(\omega,z) + \frac{\delta\beta}{\beta}(z)K_c^\beta(\omega,z)\\ &+\delta g_c(z)K_c^{g_c}(\omega,z)\cos 2\theta + \delta g_s(z)K_c^{g_s}(\omega,z)\sin 2\theta\Big]\,dz,\end{aligned} \tag{B13}$$

where the sensitivity kernels with respect to body wave velocities are related to the sensitivity kernels of elastic parameters (as listed in Table B2) by:

$$K_c^\alpha = 2\alpha^2\rho\left(K_c^A + K_c^C + K_c^F\right), \tag{B14}$$

$$K_c^\beta = 2\beta^2\rho\left(K_c^L - 2K_c^F\right), \tag{B15}$$

$$K_c^{g_c} = K_c^{g_s} = 2\beta^2\rho\left(K_c^L + K_c^A\right). \tag{B16}$$

Appendix C: Modeling Azimuthally Anisotropic Rayleigh Wave Phase Velocity by Elliptically Anisotropic Eikonal Equation

In this section, we justify the use of the elliptically anisotropic eikonal equation to model the traveltime of Rayleigh waves in azimuthally anisotropic media. As derived in Appendix B, in weak anisotropic media, the surface wave phase velocity displays azimuthal dependence and can be expressed as:

$$c(\omega,\theta) = c_0(\omega)[1 + r_1(\omega)\cos 2\theta + r_2(\omega)\sin 2\theta], \tag{C1}$$

where θ is the azimuth measured anticlockwise from the east, ω is the angular frequency, and c_0 is the phase velocity in the isotropic model. The coefficients r_1 and r_2 represent the relative amplitudes of the azimuthally dependent terms which can be expressed as:

$$r_1(\omega) = \frac{1}{c_0(\omega)}\int_0^\infty \left[g_c(z)K_c^{g_c}(\omega,z)\right]dz, \tag{C2}$$

$$r_2(\omega) = \frac{1}{c_0(\omega)}\int_0^\infty \left[g_s(z)K_c^{g_s}(\omega,z)\right]dz. \tag{C3}$$

Equation C1 can be rewritten as the summation of the isotropic phase velocity and an azimuthally dependent term:

$$c(\omega,\theta) = c_0(\omega)\left[1 + \sqrt{r_1^2(\omega)+r_2^2(\omega)}\cos 2(\theta-\phi)\right], \tag{C4}$$

where ϕ is an angle satisfying $\cos 2\phi = \frac{r_1}{\sqrt{r_1^2+r_2^2}}$ and $\sin 2\phi = \frac{r_2}{\sqrt{r_1^2+r_2^2}}$. From Equation C4, it can be observed that the fast phase velocity $\left(c_1 = c_0 + c_0\sqrt{r_1^2 + r_2^2}\right)$ occurs when the azimuth is equal to ϕ (or $\phi + \pi$), whereas the slow phase velocity $\left(c_2 = c_0 - c_0\sqrt{r_1^2 + r_2^2}\right)$ occurs when the azimuth is perpendicular to ϕ.

As discussed in Section 2.1, the propagation of surface waves exhibiting orthogonal fast and slow velocities can be described using the elliptically anisotropic eikonal equation Equation 9. This equation includes three parameters describing anisotropic surface wave slowness: s, ξ, and η, which are related to fast phase velocity, slow phase velocity, and fast velocity direction c_1, c_2, and ϕ by Equations 10–12. By substituting the definition of c_1, c_2, and ϕ into Equations 10–12, we obtain:

$$s = \frac{1}{c_0}\sqrt{\frac{1}{1 + r_1^2 + r_2^2}}, \tag{C5}$$

$$\xi = \frac{r_1}{1 + r_1^2 + r_2^2}, \tag{C6}$$

$$\eta = \frac{r_2}{1 + r_1^2 + r_2^2}. \tag{C7}$$

Based on these relationships, the perturbations of the anisotropic surface wave parameters can be expressed by the perturbations of the body wave parameters:

$$\delta s = \int_0^\infty \left[\frac{\delta\alpha}{\alpha}K_s^\alpha + \frac{\delta\beta}{\beta}K_s^\beta + \delta g_s K_s^{g_s} + \delta g_c K_s^{g_c}\right] dz, \tag{C8}$$

$$\delta\xi = \int_0^\infty \left[\delta g_c K_\xi^{g_c} + \delta g_s K_\xi^{g_s}\right] dz, \tag{C9}$$

$$\delta\eta = \int_0^\infty \left[\delta g_c K_\eta^{g_c} + \delta g_s K_\eta^{g_s}\right] dz, \tag{C10}$$

where:

$$K_s^\alpha = -\frac{1}{c_0^2}\sqrt{\frac{1}{1 + r_1^2 + r_2^2}}K_c^\alpha, \tag{C11}$$

$$K_s^\beta = -\frac{1}{c_0^2}\sqrt{\frac{1}{1 + r_1^2 + r_2^2}}K_c^\beta, \tag{C12}$$

$$K_s^{g_c} = -\frac{r_1}{c_0^2\left(1 + r_1^2 + r_2^2\right)^{\frac{3}{2}}}K_c^{g_c}, \tag{C13}$$

$$K_s^{g_s} = -\frac{r_2}{c_0^2\left(1 + r_1^2 + r_2^2\right)^{\frac{3}{2}}}K_c^{g_s}, \tag{C14}$$

$$K_\xi^{g_c} = \frac{1 - r_1^2 + r_2^2}{c_0\left(1 + r_1^2 + r_2^2\right)^2}K_c^{g_c}, \tag{C15}$$

$$K_{\xi}^{g_{\xi}} = -\frac{2r_1 r_2}{c_0\left(1 + r_1^2 + r_2^2\right)^2} K_c^{g_{\xi}}, \tag{C16}$$

$$K_{\eta}^{g_{\eta}} = \frac{1 + r_1^2 - r_2^2}{c_0\left(1 + r_1^2 + r_2^2\right)^2} K_c^{g_{\eta}}, \tag{C17}$$

$$K_{\eta}^{g_{\xi}} = -\frac{2r_1 r_2}{c_0\left(1 + r_1^2 + r_2^2\right)^2} K_c^{g_{\xi}}. \tag{C18}$$

Appendix D: Inversion of Relative Ambient Noise Source Amplitudes

Following Harmon et al. (2010), the frequency-domain cross-correlation function of ambient noise, R, can be modeled in terms of the amplitude density function $A(\theta, \omega)$ of plane waves:

$$R(\omega, t(\omega), \phi) = \frac{1}{2\pi}\int_0^{2\pi} A(\theta, \omega) e^{i\omega t(\omega)\cos(\theta - \phi)} d\theta \tag{D1}$$

$$= a_0 J_0(\omega t(\omega)) + 2\sum_{n=1}^{\infty} i^n J_n(\omega t(\omega))[a_n(\omega)\cos(n\phi) + b_n(\omega)\sin(n\phi)], \tag{D2}$$

where θ is the azimuth of incoming plane waves, ω is the angular frequency, $t(\omega)$ is the phase traveltime between two stations, ϕ is the azimuth between two stations, and J_n is the Bessel function of the first kind of order n. Equation D2 is derived from Equation D1 by applying the Jacobi–Anger expansion to the exponential term and expressing the amplitude density function $A(\theta, \omega)$ as a Fourier series. The coefficients a_n and b_n in Equation D2 are the Fourier coefficients of the amplitude density function $A(\theta, \omega)$, which can be expressed as:

$$A(\theta, \omega) = a_0 + \sum_{n=1}^{\infty}[a_n(\omega)\cos(n\theta) + b_n(\omega)\sin(n\theta)]. \tag{D3}$$

In practice, high-order terms of the Fourier series can be omitted to model a smooth amplitude density function. In this case, the ambient noise distribution can be represented by a parameter vector $\boldsymbol{m} = (a_0, a_1, b_1, \ldots, a_n, b_n)^t$. For a given frequency, the frequency-domain cross-correlation functions from multiple station pairs can be assembled into a data vector $\boldsymbol{d}$. Consequently, Equation D2 can be reformulated in matrix form as:

$$\boldsymbol{d} = \boldsymbol{G}\boldsymbol{m}, \tag{D4}$$

where $\boldsymbol{G}$ is the coefficient matrix constructed from the Bessel function terms and the azimuthal geometry of station pairs. Based on the linear relationship in Equation D4, the ambient noise source distribution can be inverted from the observed cross-correlation functions. It is important to note that both $\boldsymbol{G}$ and $\boldsymbol{d}$ are complex-valued, whereas the model vector $\boldsymbol{m}$ is real. To perform the inversion, we recast the problem using the real and imaginary components, resulting in the following damped least-squares solution:

$$\hat{\boldsymbol{m}} = \left(\boldsymbol{G}_e{}^t \boldsymbol{G}_e + \lambda \boldsymbol{D}\right)^{-1} \boldsymbol{G}_e{}^t \boldsymbol{d}_e, \tag{D5}$$

where $\boldsymbol{G}_e = \begin{bmatrix} \mathrm{Re}(\boldsymbol{G}) \\ \mathrm{Im}(\boldsymbol{G}) \end{bmatrix}$ is the extended coefficient matrix, $\boldsymbol{d}_e$ is the corresponding extended data vector that is similarly defined, and λ is the damping parameter. The damping matrix $\boldsymbol{D}$ is defined as:

Table D1
Parameters for the Modeling and Inversion of Relative Ambient Noise Source Amplitudes

Period (s)	Order of fourier series	Damping parameter (λ)
1.0	7	1,000
1.25	7	500
1.5	7	500
1.75	7	400
2.0	7	200
2.25	7	50
2.5	7	50

$$\boldsymbol{D} = \begin{bmatrix} 0 & 0 & 0 & \cdots & 0 \\ 0 & 1 & 0 & \cdots & 0 \\ 0 & 0 & 1 & \cdots & 0 \\ \vdots & \vdots & \vdots & \ddots & \vdots \\ 0 & 0 & 0 & \cdots & 1 \end{bmatrix}. \quad \text{(D6)}$$

By setting $D_{11} = 0$, the regularization leaves the zeroth-order (mean) coefficient unpenalized while damping all higher-order terms, thereby favoring an azimuthally uniform ambient-noise source distribution. Finally, phase delays caused by uneven ambient noise source distributions are evaluated. Frequency-domain cross-correlation functions are predicted using Equation D4, and the phase delays are obtained by computing the phase difference between cross-correlation functions derived from the inverted amplitude density function and those based on a uniform ambient noise distribution. In this case study at Huidong region, the parameters for the modeling and inversion of relative ambient noise source amplitudes are summarized in Table D1.

Conflict of Interest

The authors declare no conflicts of interest relevant to this study.

Availability Statement

The ambient noise cross-correlation functions and Rayleigh wave phase traveltime data supporting this study are available at Zenodo via https://doi.org/10.5281/zenodo.18476824 (Hao et al., 2026a). The source code used for the case study is archived at Zenodo via https://doi.org/10.5281/zenodo.18506146 (Hao et al., 2026b). The Generic Mapping Tools is used for making most figures (Wessel et al., 2019).

Acknowledgments
We thank the Editor and the anonymous reviewers for their constructive comments and suggestions, which significantly improved the quality of this manuscript. This work is supported by National Key R&D Plan of China (Grant 2023YFF0803301) and Ministry of Education, Singapore, under its MOE AcRF Tier-2 Grant (MOE-T2EP20124-0003). The computational work for this article was partially performed on resources of the National Supercomputing Centre (NSCC), Singapore (https://www.nscc.sg). The data acquisition is supported by Geological Survey Project of China Geological Survey (DD20190287). We thank Wang Haibo, Han Cunrui, Zhang Zhuoran, Xia Han, Shi Jing, and Lyu Tianyang for their fieldwork in deploying and maintaining of the seismic stations.

References

Aki, K., & Richards, P. G. (2002). Quantitative seismology. MIT Press.
Almqvist, B. S. G., & Mainprice, D. (2017). Seismic properties and anisotropy of the continental crust: Predictions based on mineral texture and rock microstructure. *Reviews of Geophysics*, *55*(2), 367–433. https://doi.org/10.1002/2016RG000552
Arjwech, R., Hongsresawat, S., Chaisuriya, S., Rattanawannee, J., Kanjanapayont, P., & Youngme, W. (2024). Identification and verification of the movement of the hidden active fault using electrical resistivity tomography and excavation. *Geosciences*, *14*(8), 196. https://doi.org/10.3390/geosciences14080196
Bensen, G., Ritzwoller, M., Barmin, M., Levshin, A. L., Lin, F., Moschetti, M., et al. (2007). Processing seismic ambient noise data to obtain reliable broad-band surface wave dispersion measurements. *Geophysical Journal International*, *169*(3), 1239–1260. https://doi.org/10.1111/j.1365-246x.2007.03374.x
Bensen, G. D., Ritzwoller, M. H., & Shapiro, N. M. (2008). Broadband ambient noise surface wave tomography across the United States. *Journal of Geophysical Research*, *113*(B5), B05306. https://doi.org/10.1029/2007JB005248
Bodin, T., Sambridge, M., Gallagher, K., & Rawlinson, N. (2012). Transdimensional inversion of receiver functions and surface wave dispersion. *Journal of Geophysical Research*, *117*(B2), B02301. https://doi.org/10.1029/2011JB008560
Boness, N. L., & Zoback, M. D. (2006). Mapping stress and structurally controlled crustal shear velocity anisotropy in California. *Geology*, *34*(10), 825–828. https://doi.org/10.1130/g22309.1
Chen, J., Chen, G., Nagaso, M., & Tong, P. (2023). Adjoint-state traveltime tomography for azimuthally anisotropic media in spherical coordinates. *Geophysical Journal International*, *234*(1), 712–736. https://doi.org/10.1093/gji/ggad093
Chen, M., & Tromp, J. (2007). Theoretical and numerical investigations of global and regional seismic wave propagation in weakly anisotropic earth models. *Geophysical Journal International*, *168*(3), 1130–1152. https://doi.org/10.1111/j.1365-246x.2006.03218.x
Chen, Y., de Ridder, S. A., Rost, S., Guo, Z., Wu, X., Li, S., & Chen, Y. (2023). Physics-informed neural networks for elliptical-anisotropy eikonal tomography: Application to data from the Northeastern Tibetan Plateau. *Journal of Geophysical Research: Solid Earth*, *128*(12), e2023JB027378. https://doi.org/10.1029/2023jb027378
Dai, X., Li, Z., Hu, L., Zhang, P., Yang, X., Almeida, R., & Li, G. (2024). Exploring fault geometry and Holocene deformation of the Littoral fault zone within the seismic gap south of Greater Bay Area, China. *Journal of Marine Science and Engineering*, *12*(8), 1350. https://doi.org/10.3390/jmse12081350
Datta, A., Shekar, B., & Kumar, P. L. (2023). Acoustic full waveform inversion for 2-D ambient noise source imaging. *Geophysical Journal International*, *234*(3), 1628–1639. https://doi.org/10.1093/gji/ggad158
De Ridder, S., Biondi, B., & Nichols, D. (2015). Elliptical-anisotropic eikonal phase velocity tomography. *Geophysical Research Letters*, *42*(3), 758–764. https://doi.org/10.1002/2014gl062805
Dilalos, S., & Alexopoulos, J. D. (2020). The contribution of an urban gravity survey to the determinable perspective of Athens city (Greece) underground structure. *SN Applied Sciences*, *2*(11), 1797. https://doi.org/10.1007/s42452-020-03466-8

Du, N., Yang, T., Xu, T., & Liu, Q. (2024). Incorporating topographic effects in surface wave tomography based on shortest-path ray tracing. *Geophysical Journal International*, *237*(2), 1235–1248. https://doi.org/10.1093/gji/ggae115

Eberhart-Phillips, D., & Mark Henderson, C. (2004). Including anisotropy in 3-d velocity inversion and application to marlborough, New Zealand. *Geophysical Journal International*, *156*(2), 237–254. https://doi.org/10.1111/j.1365-246x.2003.02044.x

Fang, H., Yao, H., Zhang, H., Huang, Y.-C., & van der Hilst, R. D. (2015). Direct inversion of surface wave dispersion for three-dimensional shallow crustal structure based on ray tracing: Methodology and application. *Geophysical Journal International*, *201*(3), 1251–1263. https://doi.org/10.1093/gji/ggv080

Galetti, E., Curtis, A., Baptie, B., Jenkins, D., & Nicolson, H. (2016). Transdimensional Love-wave tomography of the British Isles and shear-velocity structure of the East Irish Sea Basin from ambient-noise interferometry. *Geophysical Journal International*, *208*(1), 36–58. https://doi.org/10.1093/gji/ggw286

García, B., Guevara-Pillaca, C. J., Unsworth, M., Pereyra, P., Benavente, C., Combey, A., et al. (2025). Locating active faults in the Cusco Valley using magnetotelluric and radon gas data. *Tectonophysics*, *898*, 230639. https://doi.org/10.1016/j.tecto.2025.230639

Hao, S., Chen, J., Xu, M., & Tong, P. (2024). Topography-incorporated adjoint-state surface wave traveltime tomography: Method and a case study in Hawaii. *Journal of Geophysical Research: Solid Earth*, *129*(1), e2023JB027454. https://doi.org/10.1029/2023JB027454

Hao, S., Chen, J., Xu, M., Yu, D., Xie, J., & Tong, P. (2026a). Replication data for: "Topography-Incorporated Adjoint-State Surface Wave Traveltime Tomography for Azimuthally Anisotropic Media" [Dataset]. *Zenodo*. https://doi.org/10.5281/zenodo.18476824

Hao, S., Chen, J., Xu, M., Yu, D., Xie, J., & Tong, P. (2026b). SurfATT v1.0: Reproducible code for "Topography- Incorporated Adjoint-State Surface Wave Traveltime Tomography for Azimuthally Anisotropic Media" [Software]. *Zenodo*. https://doi.org/10.5281/zenodo.18506146

Harmon, N., Rychert, C., & Gerstoft, P. (2010). Distribution of noise sources for seismic interferometry. *Geophysical Journal International*, *183*(3), 1470–1484. https://doi.org/10.1111/j.1365-246x.2010.04802.x

Ishiyama, T., Sato, H., Abe, S., Kawasaki, S., & Kato, N. (2016). High-resolution 3D seismic reflection imaging across active faults and its impact on seismic hazard estimation in the Tokyo metropolitan area. *Tectonophysics*, *689*, 79–88. https://doi.org/10.1016/j.tecto.2016.01.042

Johnson, J. H., Savage, M. K., & Townend, J. (2011). Distinguishing between stress-induced and structural anisotropy at Mount Ruapehu volcano, New Zealand. *Journal of Geophysical Research*, *116*(B12), B12303. https://doi.org/10.1029/2011jb008308

Kao, C.-Y., Osher, S., & Tsai, Y.-H. (2005). Fast sweeping methods for static Hamilton–Jacobi equations. *SIAM Journal on Numerical Analysis*, *42*(6), 2612–2632. https://doi.org/10.1137/s0036142902419600

Kästle, E. D., El-Sharkawy, A., Boschi, L., Meier, T., Rosenberg, C., Bellahsen, N., et al. (2018). Surface wave tomography of the Alps using ambient-noise and earthquake phase velocity measurements. *Journal of Geophysical Research: Solid Earth*, *123*(2), 1770–1792. https://doi.org/10.1002/2017jb014698

Köhler, A., Weidle, C., & Maupin, V. (2012). On the effect of topography on surface wave propagation in the ambient noise frequency range. *Journal of Seismology*, *16*(2), 221–231. https://doi.org/10.1007/s10950-011-9264-5

Koulakov, I., Maksotova, G., Jaxybulatov, K., Kasatkina, E., Shapiro, N. M., Luehr, B.-G., et al. (2016). Structure of magma reservoirs beneath Merapi and surrounding volcanic centers of Central Java modeled from ambient noise tomography. *Geochemistry, Geophysics, Geosystems*, *17*(10), 4195–4211. https://doi.org/10.1002/2016gc006442

Kramer, S. L., & Stewart, J. P. (2024). *Geotechnical earthquake engineering*. CRC Press.

Larson, E. W., Tromp, J., & Ekström, G. (1998). Effects of slight anisotropy on surface waves. *Geophysical Journal International*, *132*(3), 654–666. https://doi.org/10.1046/j.1365-246x.1998.00452.x

Li, J., Cawood, P. A., Ratschbacher, L., Zhang, Y., Dong, S., Xin, Y., et al. (2020). Building Southeast China in the late Mesozoic: Insights from alternating episodes of shortening and extension along the Lianhuashan fault zone. *Earth-Science Reviews*, *201*, 103056. https://doi.org/10.1016/j.earscirev.2019.103056

Li, X., Huang, S., Hergert, T., Henk, A., & Du, Q. (2024). Contemporary crustal kinematics in the Guangdong-Hong Kong-Macao Greater Bay Area, SE China: Implications for the geothermal resource exploration. *Journal of Asian Earth Sciences*, *263*, 106041. https://doi.org/10.1016/j.jseaes.2024.106041

Li, Z., & Peng, Z. (2017). Stress-and structure-induced anisotropy in southern California from two decades of shear wave splitting measurements. *Geophysical Research Letters*, *44*(19), 9607–9614. https://doi.org/10.1002/2017gl075163

Lin, F.-C., Ritzwoller, M. H., & Snieder, R. (2009). Eikonal tomography: Surface wave tomography by phase front tracking across a regional broad-band seismic array. *Geophysical Journal International*, *177*(3), 1091–1110. https://doi.org/10.1111/j.1365-246x.2009.04105.x

Lingyan, X., Changsong, L., Xiao, L., & Yue, H. (2019). A study of extension of Lianhuashan fault in Guangdong to adjacent marine space based on remote sensing and aeromagnetic data. *Remote Sensing for Land & Resources*, *31*(1), 247–254.

Liu, C., Yao, H., Yang, H.-Y., Shen, W., Fang, H., Hu, S., & Qiao, L. (2019). Direct inversion for three-dimensional shear wave speed azimuthal anisotropy based on surface wave ray tracing: Methodology and application to Yunnan, southwest China. *Journal of Geophysical Research: Solid Earth*, *124*(11), 11394–11413. https://doi.org/10.1029/2018jb016920

Liu, L., Wang, G., Li, Y., Wei, Z., Lin, W., Qin, X., et al. (2024). Hydrogeochemistry of geothermal water in Huangshadong and adjacent areas of Guangdong province: Implications for water-rock interaction. *Geothermics*, *122*, 103084. https://doi.org/10.1016/j.geothermics.2024.103084

Liu, X., Beroza, G. C., & Li, H. (2023). Ambient noise differential adjoint tomography reveals fluid-bearing rocks near active faults in Los Angeles. *Nature Communications*, *14*(1), 6873. https://doi.org/10.1038/s41467-023-42536-4

Lobkis, O. I., & Weaver, R. L. (2001). On the emergence of the Green's function in the correlations of a diffuse field. *Journal of the Acoustical Society of America*, *110*(6), 3011–3017. https://doi.org/10.1121/1.1417528

Lü, Z., Huang, H., Ye, X., Lü, J., & Xiong, C. (2021). High-Resolution crustal shear-wave velocity structure in the Pearl River Delta, South China. *Seismological Research Letters*, *93*(1), 338–350. https://doi.org/10.1785/0220210116

Luo, Y., Yang, Y., Xu, Y., Xu, H., Zhao, K., & Wang, K. (2015). On the limitations of interstation distances in ambient noise tomography. *Geophysical Journal International*, *201*(2), 652–661. https://doi.org/10.1093/gji/ggv043

Montagner, J.-P., & Anderson, D. L. (1989). Petrological constraints on seismic anisotropy. *Physics of the Earth and Planetary Interiors*, *54*(1–2), 82–105. https://doi.org/10.1016/0031-9201(89)90189-1

Montagner, J.-P., & Nataf, H.-C. (1986). A simple method for inverting the azimuthal anisotropy of surface waves. *Journal of Geophysical Research*, *91*(B1), 511–520. https://doi.org/10.1029/jb091ib01p00511

Nishida, K. (2017). Ambient seismic wave field. *Proceedings of the Japan Academy, Series B*, *93*(7), 423–448. https://doi.org/10.2183/pjab.93.026

Porras, D., Carrasco, J., Carrasco, P., & González, P. J. (2022). Imaging extensional fault systems using deep electrical resistivity tomography: A case study of the Baza fault, Betic Cordillera, Spain. *Journal of Applied Geophysics*, *202*, 104673. https://doi.org/10.1016/j.jappgeo.2022.104673

Reeve, M. T., Bell, R. E., Duffy, O. B., Jackson, C. A. L., & Sansom, E. (2015). The growth of non-colinear normal fault systems; what can we learn from 3D seismic reflection data? *Journal of Structural Geology*, *70*, 141–155. https://doi.org/10.1016/j.jsg.2014.11.007

Sadeghisorkhani, H., Gudmundsson, Ó., Roberts, R., & Tryggvason, A. (2017). Velocity-measurement bias of the ambient noise method due to source directivity: A case study for the Swedish National Seismic Network. *Geophysical Journal International*, *209*(3), 1648–1659. https://doi.org/10.1093/gji/ggx115

Shao-Bai, X., Hong-Bing, L., You-Xue, W., Zhou-Xun, Y., Ji-Wen, T., & Hong-Xiang, H. (2002). A Study on velocity distribution in upper crust and tectonics of basement and cover in south China. *Chinese Journal of Geophysics*, *45*(6), 831–841. https://doi.org/10.1002/cjg2.298

Shapiro, N. M., Campillo, M., Stehly, L., & Ritzwoller, M. H. (2005). High-resolution surface-wave tomography from ambient seismic noise. *Science*, *307*(5715), 1615–1618. https://doi.org/10.1126/science.1108339

Smith, M. L., & Dahlen, F. (1973). The azimuthal dependence of Love and Rayleigh wave propagation in a slightly anisotropic medium. *Journal of Geophysical Research*, *78*(17), 3321–3333. https://doi.org/10.1029/jb078i017p03321

Snieder, R. (1986). The influence of topography on the propagation and scattering of surface waves. *Physics of the Earth and Planetary Interiors*, *44*(3), 226–241. https://doi.org/10.1016/0031-9201(86)90072-5

Tanimoto, T., & Anderson, A. (2023). Seismic noise between 0.003 Hz and 1.0 Hz and its classification. *Progress in Earth and Planetary Science*, *10*(1), 56. https://doi.org/10.1186/s40645-023-00587-7

Tong, P. (2021a). Adjoint-State traveltime tomography: Eikonal equation-based methods and application to the anza area in Southern California. *Journal of Geophysical Research: Solid Earth*, *126*(5), e2021JB021818. https://doi.org/10.1029/2021JB021818

Tong, P. (2021b). Adjoint-State traveltime tomography for azimuthally anisotropic media and Insight into the crustal structure of central California near parkfield. *Journal of Geophysical Research: Solid Earth*, *126*(10), e2021JB022365. https://doi.org/10.1029/2021JB022365

Tong, P., Yang, D., & Huang, X. (2019). Multiple-grid model parametrization for seismic tomography with application to the San Jacinto fault zone. *Geophysical Journal International*, *218*(1), 200–223. https://doi.org/10.1093/gji/ggz151

Tsai, V. C. (2009). On establishing the accuracy of noise tomography travel-time measurements in a realistic medium. *Geophysical Journal International*, *178*(3), 1555–1564. https://doi.org/10.1111/j.1365-246X.2009.04239.x

Tsai, Y.-H. R., Cheng, L.-T., Osher, S., & Zhao, H.-K. (2003). Fast sweeping algorithms for a class of Hamilton–Jacobi equations. *SIAM Journal on Numerical Analysis*, *41*(2), 673–694. https://doi.org/10.1137/s0036142901396533

Wang, J., Wu, G., & Chen, X. (2019). Frequency-bessel transform method for effective imaging of higher-mode rayleigh dispersion curves from ambient seismic noise data. *Journal of Geophysical Research: Solid Earth*, *124*(4), 3708–3723. https://doi.org/10.1029/2018jb016595

Wang, K., Luo, Y., & Yang, Y. (2016). Correction of phase velocity bias caused by strong directional noise sources in high-frequency ambient noise tomography: A case study in Karamay, China. *Geophysical Journal International*, *205*(2), 715–727. https://doi.org/10.1093/gji/ggw039

Wessel, P., Luis, J. F., Uieda, L., Scharroo, R., Wobbe, F., Smith, W. H. F., & Tian, D. (2019). The generic mapping tools version 6. *Geochemistry, Geophysics, Geosystems*, *20*(11), 5556–5564. https://doi.org/10.1029/2019GC008515

Woodhouse, J. (1974). Surface waves in a laterally varying layered structure. *Geophysical Journal International*, *37*(3), 461–490. https://doi.org/10.1111/j.1365-246x.1974.tb04098.x

Wu, X., Xu, X., Yu, G., Ren, J., Yang, X., Chen, G., et al. (2024). The China Active Faults Database (CAFD) and its web system. *Earth System Science Data*, *16*(7), 3391–3417. https://doi.org/10.5194/essd-16-3391-2024

Xie, J., Yang, Y., & Luo, Y. (2020). Improving cross-correlations of ambient noise using an rms-ratio selection stacking method. *Geophysical Journal International*, *222*(2), 989–1002. https://doi.org/10.1093/gji/ggaa232

Xin, Y., Li, J., Zhang, Y., & Dong, S. (2023). Episodic magmatism in the Lianhuashan tectonic belt: Implications for late Mesozoic crustal reworking in SE South China. *GSA Bulletin*, *135*(11–12), 3043–3065. https://doi.org/10.1130/B36504.1

XiuWei, Y. E., Xiang, Z., JinShui, L., BaoFeng, L. I. U., XiaoNa, W., LiWei, W., et al. (2020). Crustal structure and tectonic attribute revealed by a deep seismic sounding profile of Dinghu-Gaoming-Jinwan in the pearl river delta. *Chinese Journal of Geophysics*, *63*(5), 1959–1969. https://doi.org/10.6038/cjg2020M0378

Xu, M., Hao, S., Chen, J., Zhang, B., & Tong, P. (2025). SurfATT: High-performance package for adjoint-state surface-wave travel-time tomography. *Seismological Research Letters*, *96*(4), 2638–2646. https://doi.org/10.1785/0220240206

Yan, M., Yao, H., Lei, T., Luo, S., & Feng, J. (2024). Linear array double difference adjoint ambient noise tomography of the central tanlu Fault Zone, Eastern China. *Journal of Geophysical Research: Solid Earth*, *129*(7), e2024JB028791. https://doi.org/10.1029/2024JB028791

Yanis, M., Abdullah, F., Zaini, N., & Ismail, N. (2021). The northernmost part of the Great Sumatran Fault map and images derived from gravity anomaly. *Acta Geophysica*, *69*(3), 795–807. https://doi.org/10.1007/s11600-021-00567-9

Yao, H., & Van Der Hilst, R. D. (2009). Analysis of ambient noise energy distribution and phase velocity bias in ambient noise tomography, with application to SE Tibet. *Geophysical Journal International*, *179*(2), 1113–1132. https://doi.org/10.1111/j.1365-246x.2009.04329.x

Yao, H., van der Hilst, R. D., & de Hoop, M. V. (2006). Surface-wave array tomography in SE Tibet from ambient seismic noise and two-station analysis - I. Phase velocity maps. *Geophysical Journal International*, *166*(2), 732–744. https://doi.org/10.1111/j.1365-246X.2006.03028.x

Zhang, C., Li, B., Li, H., He, M., Gan, H., Wang, G., & Fan, Y. (2023). Stress estimation in a 3 km-deep geothermal borehole: A snapshot of stress state in Southern Cathaysia block, China. *Tectonophysics*, *864*, 230031. https://doi.org/10.1016/j.tecto.2023.230031

Zhou, C., Xia, J., Cheng, F., Pang, J., Chen, X., Xing, H., & Chang, X. (2022). Passive surface-wave waveform inversion for source-velocity joint imaging. *Surveys in Geophysics*, *43*(3), 853–881. https://doi.org/10.1007/s10712-022-09691-7

Zhou, X., Lan, H., Chen, L., Guo, G., Bin Waheed, U., & Badal, J. (2023). A topography-dependent eikonal solver for accurate and efficient computation of traveltimes and their derivatives in 3d heterogeneous media. *Geophysics*, *88*(2), U17–U29. https://doi.org/10.1190/geo2021-0799.1

Zhu, H., Bozdağ, E., & Tromp, J. (2015). Seismic structure of the european upper mantle based on adjoint tomography. *Geophysical Journal International*, *201*(1), 18–52. https://doi.org/10.1093/gji/ggu492

References From the Supporting Information

Wdowinski, S., Smith-Konter, B., Bock, Y., & Sandwell, D. (2007). Diffuse interseismic deformation across the Pacific–North America plate boundary. *Geology*, *35*(4), 311–314. https://doi.org/10.1130/G22938A.1